



Citrate-based materials fuel human stem cells by metabonegenic regulation

Chuying Ma^{a,b,c}, Xinggui Tian^{d,e}, Jimin P. Kim^{a,b,c}, Denghui Xie^{a,b,c,d}, Xiang Ao^{d,e}, Dingying Shan^{a,b,c}, Qiaoling Lin^{a,b,c}, Maria R. Hudock^{a,b,c}, Xiaochun Bai^{d,e,1}, and Jian Yang^{a,b,c,1}

^aDepartment of Biomedical Engineering, The Pennsylvania State University, University Park, PA 16801; ^bMaterials Research Institute, The Pennsylvania State University, University Park, PA 16801; ^cThe Huck Institutes of the Life Sciences, The Pennsylvania State University, University Park, PA 16801; ^dAcademy of Orthopedics, Guangdong Province, Guangdong Provincial Key Laboratory of Bone and Joint Degenerative Diseases, The Third Affiliated Hospital of Southern Medical University, Guangzhou 510280, China; and ^eDepartment of Cell Biology, School of Basic Medical Sciences, Southern Medical University, Guangzhou 510515, China

Edited by David A. Weitz, Harvard University, Cambridge, MA, and approved October 22, 2018 (received for review July 27, 2018)

A comprehensive understanding of the key microenvironmental signals regulating bone regeneration is pivotal for the effective design of bioinspired orthopedic materials. Here, we identified citrate as an osteopromotive factor and revealed its metabonegenic role in mediating citrate metabolism and its downstream effects on the osteogenic differentiation of human mesenchymal stem cells (hMSCs). Our studies show that extracellular citrate uptake through solute carrier family 13, member 5 (SLC13a5) supports osteogenic differentiation via regulation of energy-producing metabolic pathways, leading to elevated cell energy status that fuels the high metabolic demands of hMSC osteodifferentiation. We next identified citrate and phosphoserine (P_{Ser}) as a synergistic pair in polymeric design, exhibiting concerted action not only in metabonegenic potential for orthopedic regeneration but also in facile reactivity in a fluorescent system for materials tracking and imaging. We designed a citrate/phosphoserine-based photoluminescent biodegradable polymer (BPLP-P_{Ser}), which was fabricated into BPLP-P_{Ser}/hydroxyapatite composite microparticulate scaffolds that demonstrated significant improvements in bone regeneration and tissue response in rat femoral-condyle and cranial-defect models. We believe that the present study may inspire the development of new generations of biomimetic biomaterials that better recapitulate the metabolic microenvironments of stem cells to meet the dynamic needs of cellular growth, differentiation, and maturation for use in tissue engineering.

metabonegenic regulation | energy metabolism | citrate-based materials | phosphoserine | stem cells

Bone regeneration represents a substantial component of clinical practice with more than 2 million cases of bone grafting performed each year worldwide (1) for the treatment of nonunion defects, trauma-related injuries, congenital defects, and tumor excision as well as problems resulting from metabolic disorders such as obesity and diabetes mellitus. Although significant progress has been made in the development of orthopedic biomaterials, existing materials are limited by poor mimicking of the native bone and often lack the biochemical and biological coordination necessary to mediate complex bone healing (2). Thus, a deeper understanding of the microenvironmental signals involved in bone repair, including the concerted actions of growth factors, extracellular matrix (ECM) topography, and mechanical stimuli (2), could be pivotal in guiding the design of materials that encourage stem cell differentiation and bone formation to improve healing outcomes. Emerging studies have placed a spotlight on metabolic factors in the cell microenvironment of bone, including O₂ (3), glucose (4), and glutamine (5), uncovering previously neglected factors that play distinctive roles in stem cell development and differentiation. For example, metabolic factors such as glucose have been shown to regulate the energy needs of stem cells during osteoblast differentiation, whereas factors leading to an energy deficit largely impair bone formation (4). Still, a full picture of the

metabolic processes guiding or supporting osteogenic differentiation is far from complete, as exemplified by the inadequate understanding of the role of citrate, an intermediary of cellular metabolism (6–8), in bone.

Citrate is a strongly bound and integral component that is crucial for native bone; over 90% of the body's total citrate content is stored in bone matrix and is released during bone resorption (9). As a key intermediate metabolite in the tricarboxylic acid (TCA) cycle, citrate also plays crucial regulatory roles in maintaining cell energy homeostasis (6, 7); therefore, citrate homeostasis must be tightly controlled. Intriguingly, recent studies have reported that the membrane transporter responsible for citrate uptake from the extracellular milieu, solute carrier family 13 member 5 (*SLC13a5*), is upregulated during early-stage osteointegration and active bone formation in response to mechanical loading (10, 11). The incorporation of citrate into biomaterials has also been found to enhance bone formation (12–14). These studies support the influence of exogenous citrate supplementation in osteogenic processes. However, a comprehensive understanding of the effect of citrate in osteodifferentiation is lacking, and the link between the role of

Significance

Differentiation of mesenchymal stem cells (MSCs) to bone-forming cells is central to bone regeneration, the extent of which is largely regulated by microenvironment factors. Here, we find that citrate as a metabolic factor that is abundant in bone can be consumed by MSCs to fuel osteogenesis by regulating metabolic pathways. We explored the mechanism of citrate benefit and designed a biomimetic citrate-based material that could provide a citrate- and phosphoserine-rich environment during degradation based on the previously unexplored concerted action between the two bioactive factors in accelerating bone regeneration. Together, these studies open up avenues for the study of stem cell biology and design of bone biomaterials to treat critically sized defects and bone disorders of metabolic origin.

Author contributions: C.M., X.T., X.B., and J.Y. designed research; C.M., X.T., J.P.K., D.X., X.A., D.S., Q.L., and M.R.H. performed research; C.M., X.T., J.P.K., D.S., X.B., and J.Y. analyzed data; and C.M., J.P.K., and J.Y. wrote the paper.

Conflict of interest statement: J.Y. and The Pennsylvania State University have a financial interest in Acuitive Technologies, Inc. These interests have been reviewed by the University's Institutional and Individual Conflict of Interest Committees and are currently being managed by the University.

This article is a PNAS Direct Submission.

Published under the PNAS license.

¹To whom correspondence may be addressed. Email: jxy30@psu.edu or baixc15@smu.edu.cn.

This article contains supporting information online at www.pnas.org/lookup/suppl/doi:10.1073/pnas.1813000115/-DCSupplemental.

Published online November 26, 2018.

extracellular citrate in cellular metabolism and its eventual role in osteogenic differentiation has yet to be established.

Here, we identify this central link in which extracellular citrate, taken up through SLC13a5, mediates the metabolic regulation of cellular energy status that influences the progression of human mesenchymal stem cells (hMSCs) to an osteophenotype, an effect referred to as “metabonegenic regulation” (Fig. 1). Inspired by this breakthrough model, we designed a citrate-based orthopedic biomaterial based on the following rationale. (i) We identified phosphoserine (Pser), an organic phosphate donor involved in biomineralization, as an osteopromotive factor that uniquely exhibited concerted action with citrate to elevate intracellular ATP levels of hMSCs differentiating toward osteogenesis. (ii) Following on our previous work on the fluorescent mechanisms of biodegradable photoluminescent polymers (BPLPs) (15), we designed a facile, one-pot synthesis from citrate, Pser, and a diol to produce a brightly photoluminescent polymer that would enable both a multitude of imaging functionalities and the controlled release of the bioactive factors citrate and Pser from a biodegradable platform. (iii) The resulting photoluminescent biodegradable polymer, BPLP-Pser, was further fabricated into BPLP-Pser/hydroxyapatite (HA) microparticle (MP) scaffolds exhibiting biomimetic Pser-rich bioactive surfaces for improved tissue response and early bone deposition (14, 16). Broadly, these findings may transform the current understanding of cell metabolism and energy homeostasis from being bystanders to being pivotal factors guiding osteogenic stem cell differentiation (2) and may inform the future design of biomimetic orthopedic materials.

Results

Citrate as an Osteopromotive Factor Enhances Osteophenotype Progression. We first sought to uncover the role of citrate that is released from biomaterials (12, 13) in the osteogenic differentiation of hMSCs into osteoblasts. Growth medium (GM) supplemented with exogenous citrate at different dosages (0–2,000 μ M citrate, pH 7.4) showed little increase in hMSC proliferation and an absence of calcium deposition as shown by Alizarin Red staining (SI Appendix, Fig. S1A and B). In contrast, citrate supplementation in osteogenic (OG) medium revealed a dose-dependent elevation of osteogenic markers (SI Appendix,

Fig. S1B–E), indicating citrate has an osteopromotive role only after osteodifferentiation is initiated. Among the citrate concentrations studied, 200 μ M was identified as the optimal dosage for exogenous citrate supplementation based on alkaline phosphatase (ALP) and osteopontin (OPN) expression (SI Appendix, Fig. S1C–E). The osteopromotive effect of citrate was confirmed by real-time PCR (Fig. 2A), which showed remarkably elevated expression of Runx-related transcription factor 2 (*Runx2*), the earliest master determinant of osteogenesis, as well as the genes encoding bone matrix proteins such as *Colla1* (encoding collagen type 1 alpha 1) and *SPPI* (encoding OPN) in the 200- μ M citrate treatment group compared with the OG control group after 7 and 14 d. Consistently, ELISA tests (Fig. 2B) showed favorable accumulation of Runx2 protein with citrate treatment as early as day 4.

Osteogenic differentiation is a three-stage process of proliferation, matrix maturation, and mineralization (Fig. 2C). To investigate the differentiation-stage dependence of the citrate effect, we restricted citrate (200 μ M) supplementation to one of three time periods (group I: days 0–4; group II: days 4–14; and group III: days 14–21) corresponding to each stage of differentiation, plus a pretreatment period before osteoinduction (group IV). Notably, early citrate supplementation at only the proliferation stage (group I) significantly elevated ALP production at day 7 (SI Appendix, Fig. S1F), and the osteogenic effects of this early treatment were well sustained through day 14 (Fig. 2D). In contrast, late citrate supplementation during the mineralization stage (group III) exhibited diminished cumulative osteopromotive potential compared with the other groups as measured by total calcium/protein ratio after 21 d (Fig. 2D), highlighting the important role of citrate treatment at the early stages of osteogenic differentiation. Surprisingly, even citrate pretreatment in growth medium for 4 d before osteogenic induction greatly improved the downstream osteophenotype progression, as shown by increased ALP production and higher calcium/protein ratios (Fig. 2E). These exciting results indicated that exogenous citrate is an osteopromotive factor with a dosage dependence centered around 200 μ M and timing dependence favoring supplementation at early stages.

Citrate Enhances Osteophenotype Progression Through SLC13a5.

Because protein synthesis and altered metabolic activity precede and cross-talk with Runx2 expression for orchestrated osteophenotype progression in cells of osteoblast lineage (4, 5), we were excited to discover that protein synthesis increased significantly in hMSCs pretreated with citrate for 24 or 96 h compared with the respective control groups without citrate in the GM (Fig. 3A). The protein synthesis inhibitor cycloheximide (Chx) as a negative control and Torin 1 as an mTOR inhibitor abolished this activity, revealing the mTOR dependence of citrate-mediated protein synthesis. Given these findings, together with citrate’s role as a key metabolite for regulating cell energy metabolism (6–8, 17), we proposed a metabonegenic model in which exogenous citrate mediates intracellular metabolic events in preparation for osteogenic differentiation.

To set the groundwork for testing this model, we next demonstrated that the uptake of extracellular citrate is linked to downstream osteogenic processes by identifying and validating the transport mechanism involved. First, we performed a citrate assay (SI Appendix, Fig. S2A) showing a marked increase in the intracellular citrate of hMSCs upon 24 h incubation with citrate-supplemented medium, thus affirming that exogenous citrate is indeed taken up by cells because little endogenous citrate is produced by hMSCs, which rely mostly on glycolysis. Using Western blotting, we next studied the expression of the citrate plasma membrane transporter SLC13a5 before and after osteogenesis of hMSCs. We discovered that SLC13a5 expression was greatest in undifferentiated and early-stage differentiating hMSCs, gradually decreasing after 4 d of differentiation (Fig. 3B). Importantly,

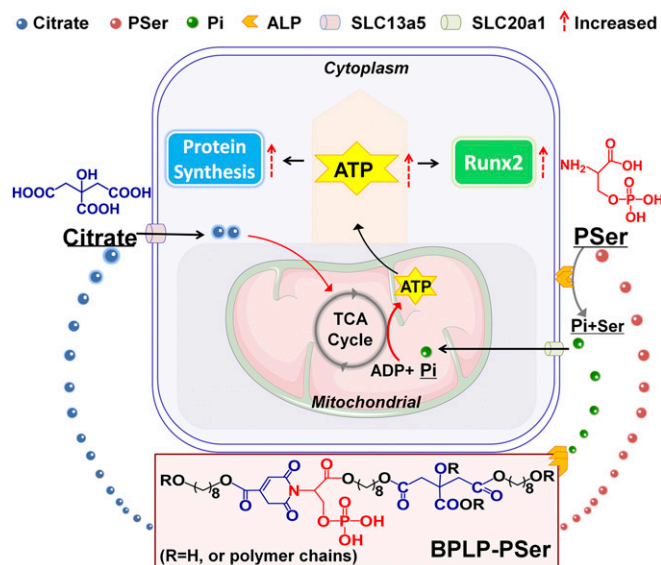


Fig. 1. Schematic model of the metabonegenic citrate-based material BPLP-Pser, which induces concerted citrate/Pser-mediated regulation of cell energy metabolism toward osteophenotype progression. Pi, inorganic phosphate.

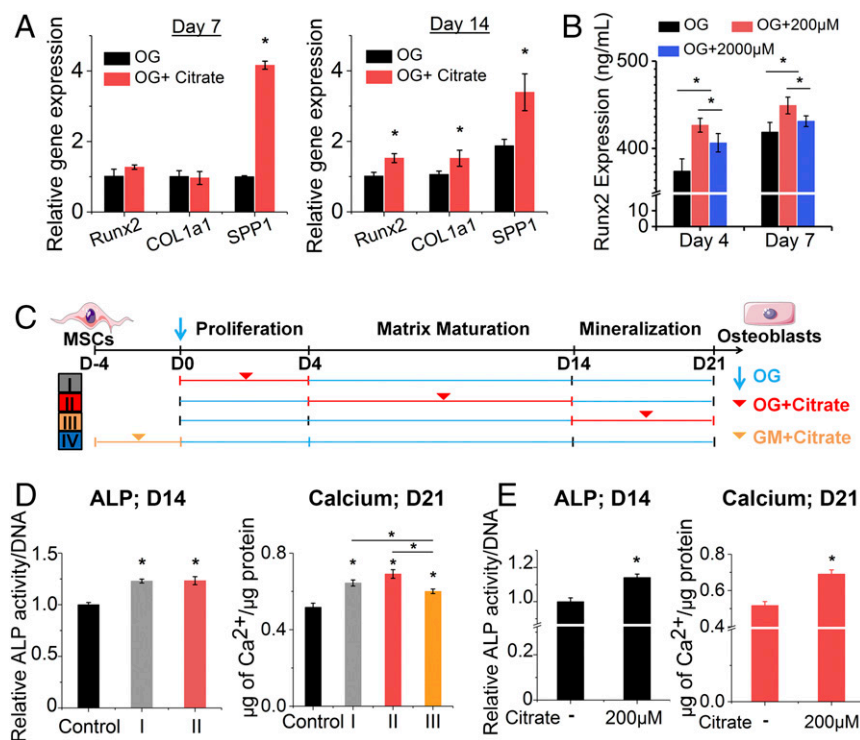


Fig. 2. The osteopromotive effect of solute citrate. (A) Gene expression of *Runx2*, *COL1a1*, and *SPP1* in differentiating hMSCs with/without citrate supplementation at 200 μ M in established OG medium for 7 and 14 d, as determined by real-time PCR. Data are shown as the expression of target genes after normalization relative to corresponding control groups without citrate supplementation at day 7 (value set to 1.0). (B) Expression of Runx2 transcription factor in hMSCs with/without citrate supplementation in OG medium as determined by ELISA. In A and B, $n \geq 4$ biological replicates per group. (C) Schematic illustration of the experimental design studying differentiation-stage dependence by restricting citrate supplementation (200 μ M) only at the proliferation stage (group I; days 0–4), the matrix maturation stage (group II; days 4–14), the mineralization stage (group III; days 14–21), or after 4 d in GM before osteoinduction (group IV; day –4 to day 0). (D) ALP expression at day 14 and calcium content in hMSCs at day 21 in OG medium supplemented with citrate only at specific differentiation stages (groups I, II, and III). (E) ALP production and calcium content in hMSCs with/without 4 d of citrate pretreatment in GM before being subjected to osteogenic differentiation in OG medium without citrate addition (group IV). In D and E, $n = 3–5$ biological replicates per group. All data are presented as mean \pm SD; * $P < 0.05$.

the addition of PF06761281, an inhibitor of SLC13a5, negated the citrate-induced elevation of ALP production (Fig. 3C). Together, these results show that exogenous citrate enters hMSCs through SLC13a5, affecting downstream osteophenotype progression, thus prompting us to further examine the metabolic events leading to osteogenesis.

Citrate Elevates Intracellular ATP by Metabolic Regulation. In response to osteostimulation, hMSCs undergo a metabolic switch from glycolysis to oxidative respiration to generate more ATP (18), since the production of abundant matrix proteins during bone formation involves high energy demands (5). We investigated the role of soluble citrate in hMSC energy metabolism and specifically asked whether citrate, as a metabolic regulator, affects the cell energy status by regulating primary energy-generating metabolic flux. After 24 h of citrate treatment, hMSCs exhibited elevated intracellular ATP levels (Fig. 3D) and an increased oxygen consumption rate (OCR) (Fig. 3E)—key indicators of mitochondrial respiration—accompanied by a decrease in glycolytic flux, indicating the inhibition of glycolysis (Fig. 3F), and reduced production of lactate (Fig. 3G), the end product of glycolysis. Therefore we propose that exogenous citrate facilitates the metabolic shift in hMSCs from glycolysis to oxidative respiration to induce higher intracellular ATP synthesis. Importantly, the effect of citrate on metabolic flux, i.e., elevating intracellular ATP levels, could be abolished by blocking SLC13a5 with the inhibitor PF06761281 (Fig. 3D–G), suggesting that the regulatory effect of exogenous citrate on cell energy

metabolism is also mediated by SLC13a5. Moreover, citrate treatment of hMSCs differentiated for 14 d elicited significant effects on intracellular ATP only after 4 d of treatment (*SI Appendix*, Fig. S2B), whereas only 1 d of treatment markedly increased hMSC mitochondrial respiration (*SI Appendix*, Fig. S2C), which was likewise abolished with the inhibitor PF06761281. However, the 1-d citrate treatment had no significant effect on glycolytic flux (*SI Appendix*, Fig. S2D). Taking these results together with our findings that citrate treatment promotes mTOR-dependent protein synthesis and favors Runx2 accumulation, we propose a previously unexplored pathway of citrate metabonegenic regulation through which exogenous citrate enters hMSCs through SLC13a5 to regulate cell energy metabolism, elevating cellular energy levels that in turn facilitate osteophenotype progression (Fig. 1).

PSer Prolongs Citrate’s Osteopromotive Effect via Concerted Citrate/PSer Metabonegenic Regulation. PSer is a functional moiety that is abundant in the noncollagenous proteins (NCPs) of natural bone. Importantly, PSer is osteopromotive (19, 20) mainly by serving as an organic phosphate donor through which ALP produces inorganic phosphate, the primary substrate for ATP production (21). Therefore, to further examine the effects of PSer on the citrate-elevated cell energy status, we treated undifferentiated hMSCs with citrate, PSer, or both. The addition of PSer exerted no significant effect on the intracellular ATP levels of hMSCs with or without citrate treatment (Fig. 3H), indicating that PSer has no direct influence on metabonegenic processes,

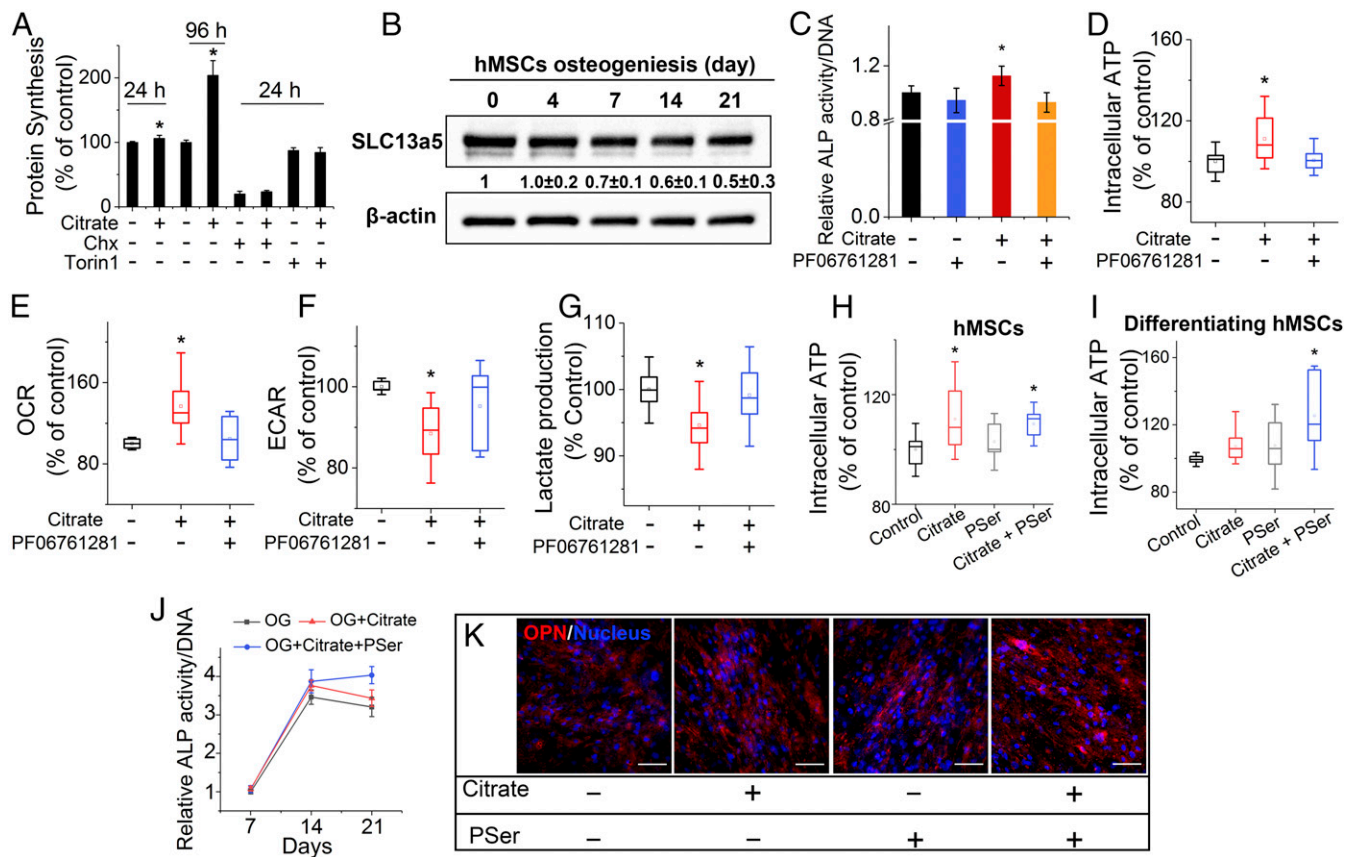


Fig. 3. Citrate metabonegenic regulation and concerted action between citrate and P5er. (A) Protein synthesis of hMSCs with 200 μ M citrate, Chx, or Torin 1 supplementation in GM for 1 and 4 d. (B) Western blot of SLC13a5 expression in hMSCs during osteogenic differentiation. (C) ALP production of hMSCs after 14 d of differentiation in OG medium supplemented with citrate, the SLC13a5 inhibitor PF06761281, or both. In A–C, $n = 3$ –5 biological replicates per group. (D) Intracellular ATP determination. (E) OCR study. (F) Extracellular acidification rate (ECAR) study. (G) Lactate production of undifferentiated hMSCs with 1 d of treatment with citrate and SLC13a5 in GM. In D–G, $n \geq 8$ biological replicates per group. (H and I) Intracellular ATP determination of hMSCs (H) and differentiating hMSCs (I) supplemented with citrate, P5er, or both in GM or OG medium, respectively. In H and I, $n = 6$ –8 biological replicates per group. (J) ALP production of differentiating hMSCs after 7, 14, and 21 d of differentiation in OG medium supplemented with citrate or with citrate and P5er. $n = 4$ biological replicates per group; all data are presented as mean \pm SD; * $P < 0.05$. (K) Immunofluorescent staining of OPN (red) with DAPI nuclear counterstain (blue) expression after 21 d of differentiation in OG medium supplemented with citrate, P5er, or both. The plus (+) and minus (–) symbols denote the presence and absence, respectively, of citrate and other specific chemicals in GM/OG medium. (Scale bars: 100 μ m.)

likely because the low levels of phosphatases present in undifferentiated cells render exogenous P5er biologically inactive. Specifically, ALP, expressed abundantly in osteoblasts, is known to hydrolyze soluble (22) or chemically bound P5er (23) to release inorganic phosphates. Indeed, there was a marked increase of intracellular ATP in differentiating hMSCs treated with the citrate and P5er combination, whereas individual treatments showed no difference from the OG medium control (Fig. 3I). Additionally, given that citric acid can react with amino acids to generate a family of citrate-based photoluminescent dyes (CPDs) (24), small-molecule citric acid-P5er (CA-P5er) was synthesized, and its effect on cell energy level was examined. There was no significant increase in the ATP level in hMSCs after 24-h treatment with CA-P5er, indicating the importance of citrate in its monomeric form for metabonegenic regulation (SI Appendix, Fig. S2E), probably because only monomeric citrate can be taken up through SLC13a5 and used for metabolic purposes.

Interestingly, the osteopromotive effects of dual treatment with citrate and P5er were particularly evident at late stages of osteogenesis, sustaining high levels of ALP (Fig. 3J and SI Appendix, Fig. S2F) and OPN production (Fig. 3K) well into day 21, whereas the ALP level dropped off in the citrate-only and control treatment groups. Even a low dosage of 40 μ M P5er [lower than the reported effective dosage (19, 20)] substantially en-

hanced the citrate-promoted osteophenotype progression, with higher P5er dosages resulting in further elevation of ALP production (SI Appendix, Fig. S2G). These findings suggest that citrate-induced elevation of ALP levels in differentiating cells catalyzes the dephosphorylation of P5er, thereby liberating the bioactive inorganic phosphate from P5er, while exogenous P5er in turn favorably prolongs the metabonegenic effect of citrate, facilitating intracellular ATP synthesis to fuel osteophenotype progression (Fig. 1).

BPLP-P5er Is a Biodegradable Photoluminescent P5er- and Citrate-Based Polymer. This identification of concerted osteopromotive action by citrate and P5er enabled us to design bioinspired polymers in which the incorporation of P5er in citrate-based polymers may mimic the bioactive NCP-rich interface layer typically used on implant surfaces to facilitate mineral deposition and regulate bone cell activities (25, 26). To prepare BPLP-P5ers, we reacted O-Phospho-DL-serine with citric acid and 1,8-octanediol via a previously described one-pot condensation reaction (15) to prepare the prepolymer, which could be further postpolymerized to generate an elastomeric cross-linked polymer network (SI Appendix, Fig. S3A). The P5er incorporation was next confirmed by 31 P-NMR (NMR, SI Appendix, Fig. S3B). HPLC analysis further verified the presence of P5er in both the

accelerated degradation product and the release medium of BPLP-PSer films (*SI Appendix, Fig. S3 C and D*), while phosphate assay of cross-linked films demonstrated the release of inorganic phosphate from the incorporated PSer in BPLP-PSer after ALP treatment (*SI Appendix, Fig. S3E*).

BPLP-PSer emitted strong fluorescence with excellent photostability (*SI Appendix, Fig. S3 F and G*), and the wavelength of the fluorescence emission was tunable by changing the excitation wavelength (Fig. 4A), consistent with the described previously band-shifting behavior of the dioxopyridine (DPR) family of CPDs and BPLPs represented by CA-Ser and BPLP-Ser (15, 24), while the fluorescence intensity was tunable by changing the molar ratio of PSer (Fig. 4B). Similar to BPLP-Ser, the fluorescence of BPLP-PSer may be attributed to the DPR structure (15, 24) generated by a key condensation step between citrate and PSer. To demonstrate the feasibility of fluorescence tracking, we measured the gradual decay of the total fluorescence signal of BPLP-PSer films using the Maestro EX in vivo imaging system (Fig. 4C), which was accompanied by a corresponding increase in accumulated fluorescent signals in the degradation solution over the same (accelerated) degradation time (Fig. 4D). Moreover, the mass-remaining profile by conventional gravimetric analysis coincided with the remaining total fluorescence profile (Fig. 4E), indicating that the degradation of BPLP-PSer could be reliably tracked by either the fluorescence remaining in polymer films or the fluorescent moiety released from the polymer films over time. The mass-remaining profile of polymer degradation in accelerated (basic) conditions (*SI Appendix, Fig. S3H*) and in PBS (pH = 7.4) (*SI Appendix, Fig. S3I*) consistently

revealed how the introduction of PSer impacted the degradation of the resultant polymers. BPLP-PSer films degraded more slowly than poly(octamethylene citrate) (POC) films but faster than BPLP-Ser films. As the tunable degradability of BPLPs has been demonstrated previously by varying the ratio of the monomers and the cross-linking conditions (15), BPLP-PSer may be designed to obtain the optimum degradation rate to meet the needs of specific applications.

Incorporated PSer Facilitates Mineral Deposition and Improves Cytocompatibility. To evaluate surface bioactivity for mineralization, we performed an in vitro mineralization assay by immersing cross-linked BPLP-PSer films in simulated body fluid, with poly (DL-lactide-co-glycolide) (PLGA) 75/25 as a general control along with POC and BPLP-Ser (incorporating L-serine) as citrate-based material controls. BPLP-PSer films displayed accelerated mineral deposition compared with all controls (*SI Appendix, Fig. S4*), indicating that PSer is a key monomer for facilitating mineralization in citrate-based polymer formulations. This result was further confirmed by a follow-up mineralization assay using polymer/50% HA (*SI Appendix, Fig. S5A*). In mechanical evaluations, the BPLP-PSer/50% HA composites possessed an impressive compressive strength of ~200 MPa (*SI Appendix, Fig. S5B*), falling into the range of human cortical bone (100–230 MPa) and suggesting strong potential in orthopedic applications. BPLP-PSer also improved the maximum HA-binding capability (up to 60%) compared with BPLP-Ser (*SI Appendix, Fig. S5B*); notably, BPLP-PSer/60% HA improved the modulus twofold compared with the BPLP-PSer/50% HA composition.

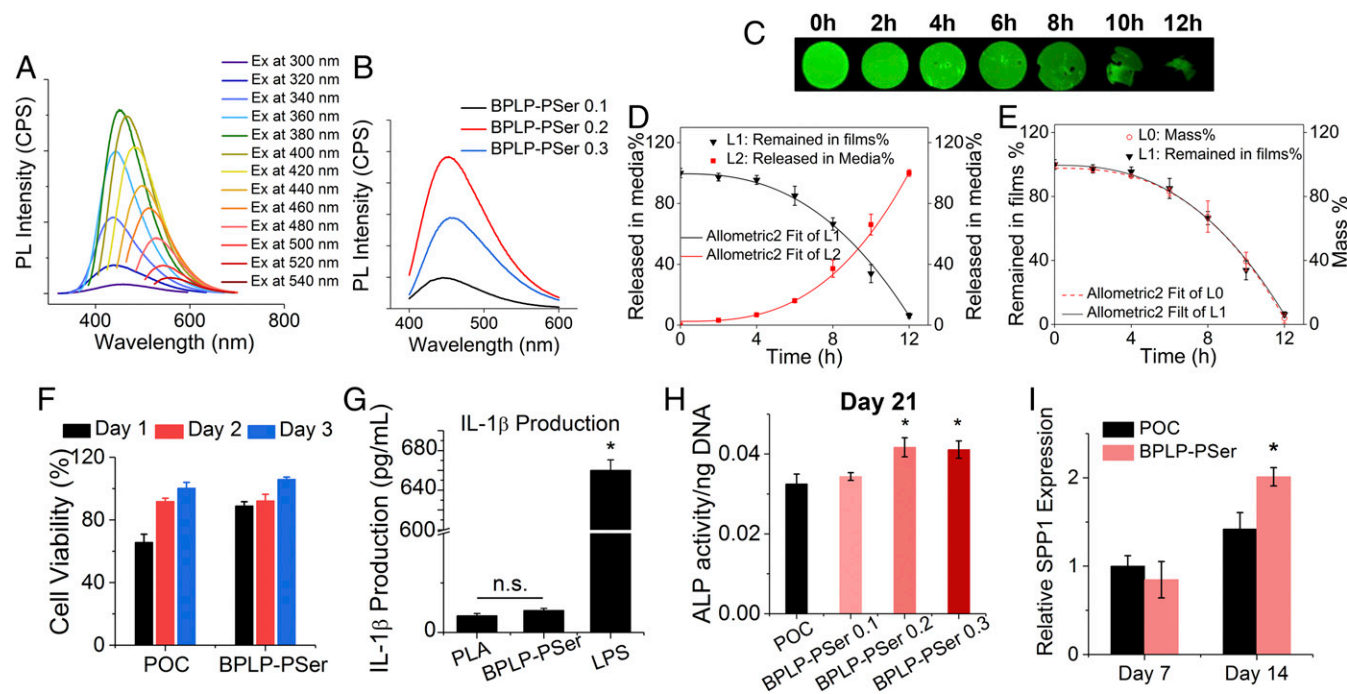


Fig. 4. BPLP-PSer as a biocompatible photoluminescent biodegradable polymer. (A) Emission spectra of BPLP-PSer-0.2 prepolymer displaying tunable emission wavelengths by changing the excitation wavelength. (B) Emission spectra of BPLP-PSer prepolymer solutions with various molar ratios of PSer excited at 370 nm. (C) Fluorescent images of BPLP-PSer films after accelerated degradation for a predetermined time (0, 2, 4, 6, 8, 10, or 12 h) in 0.05 M NaOH solution. (D) Quantitative analysis of the remaining fluorescent signal in BPLP-PSer films (L1) and the corresponding fluorescent signal in degradation medium released from polymer films (L2). (E) Comparison of the remaining-fluorescence profile of BPLP-PSer films (L1) with the conventional mass-remaining profile (L0). In C–E, $n = 5$ films per time point. (F) Cytotoxicity test on leachable extracts from polymer films. L929 cells examined by Cell Counting Kit-8 (CCK-8) show significantly greater cell viability in the BPLP-PSer group than in the POC group. (G) Release of inflammatory factor IL-1 β from THP-1 monocytes activated by incubation with polymer films, determined by ELISA. (H) ALP production of differentiating hMSCs cultured in OG medium on polymer films. BPLP-PSer 0.1/0.2/0.3 indicates 0.1, 0.2, or 0.3 molar ratios of PSer to citrate. (I) Expression of *SPP1* encoding OPN by differentiating hMSCs cultured on polymer films in OG medium. Data are shown as the relative expression of *SPP1* after normalization to the corresponding control group without citrate supplementation at day 7 (set to 1). In F–I, $n = 3$ –5 biological replicates per group. All data are presented as mean \pm SD; * $P < 0.05$; n.s., not significant.

The cytocompatibility of BPLP-PSer was systematically evaluated on leachable extracts (Fig. 4F) and degradation products (SI Appendix, Fig. S6A) and by direct contact on films (SI Appendix, Fig. S6B), demonstrating cell viabilities comparable with those of the PLGA control. ELISA studies further showed that the release of the inflammatory factor IL-1 β from THP-1 monocytes induced by BPLP-PSer films was equivalent to that induced by the polylactic acid (PLA) control (Fig. 4G and SI Appendix, Fig. S6C). Furthermore, BPLP-PSer film compositions with varying PSer content (0.1–0.3 molar ratios to citrate) were all shown to support hMSC proliferation (SI Appendix, Fig. S6D) and osteogenic differentiation, with the BPLP-PSer-0.2 and BPLP-PSer-0.3 compositions significantly elevating ALP production by day 21 (Fig. 4H and SI Appendix, Fig. S6E) and BPLP-PSer 0.2 exhibiting significantly higher OPN gene expression by day 14 (Fig. 4I) than its POC counterpart.

BPLP-PSer/HA Microparticles with Ridge-and-Cliff Surface Features Support hMSC Adhesion and Proliferation. To translate the concerted osteopromotive actions of citrate and PSer into a biomimetic material for orthopedic applications, we developed a composite MP scaffold from a porous BPLP-PSer/50% HA scaffold (150- to 250- μ m pore size by salt leaching) (SI Appendix, Fig. S7A) ground and sieved into 250- to 425- μ m microparticles (Fig. 5A). The procedure was repeated for the POC/50% HA control, although the PLGA/HA control could only incorporate up to 30% of HA for MP preparation. The BPLP-PSer/HA MPs demonstrated excellent handling ability, mixing easily with saline solution (SI Appendix, Fig. S7B and C), sodium hyaluronate carrier (SI Appendix, Fig. S7D), or blood from patients to facilitate surgical applications. The resulting BPLP-PSer/HA MPs greatly supported hMSC adhesion as examined by SEM, revealing that cells adhered abundantly to the cliff and ridge as well as to the groove structures (SI Appendix, Fig. S7E and F) of MPs after 6 h of continuous mixing of MPs and suspended hMSCs. In addition, BPLP-PSer/HA MPs supported immediate and earlier proliferation of hMSCs compared with POC/HA MPs (SI Appendix, Fig. S7G). More importantly, hMSCs cultured on POC/HA and BPLP-PSer/HA for 4 d showed a substantial increase in intracellular ATP, almost twice that of PLGA/HA MPs (Fig. 5B), likely due to innate citrate metabonegenic regulation in both citrate-based MPs, whereas PSer incorporation did not provide additional benefits to undifferentiated hMSCs, as expected.

BPLP-PSer/HA MPs Promotes hMSC Differentiation. We further examined whether citrate- and PSer-presenting MPs could exert concerted action on osteogenic progression by employing 3D Transwells (pore size: 3 μ m) as an in vitro cavity-defect model into which different MP formulations were inserted and cultured with hMSCs. Notably, even in the absence of osteogenic inducers, hMSCs in GM showed significantly higher ALP expression in the BPLP-PSer/HA group than in the POC/HA group (Fig. 5C and SI Appendix, Fig. S7H). In OG medium hMSCs in the BPLP-PSer/HA MP group displayed a substantial elevation of ALP expression by day 21 (Fig. 5D), outperforming those in the PLGA control group and even those in the citrate-only POC control group, supporting the notion that citrate and PSer may collaborate to elicit sustained bone-forming activities. Of note, as osteodifferentiation progressed, the MPs were integrated by cells to form fluorescent bone-like tissue constructs (Fig. 5F and SI Appendix, Fig. S8A) that remained intact upon compression and recovered upon unloading (Movie S1) and that had increased compressive strength and modulus (Fig. 5E and SI Appendix, Fig. S8B). By designing polydimethylsiloxane (PDMS) culture wells in the shape of the letters P, S, and U, we succeeded in generating P-, S-, and U-shaped fluorescent constructs (Fig. 5F), demonstrating the attractive potential of MPs to fill and bridge irregular defects. In fact, SEM revealed a thick layer of cells covering MP surfaces and bridging together adjacent MPs (SI Appendix, Fig.

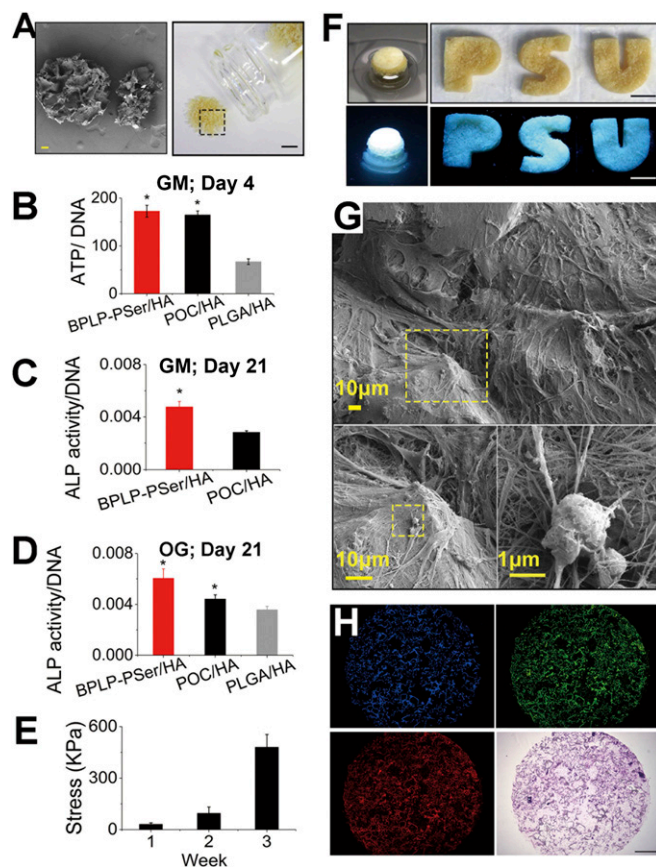


Fig. 5. BPLP-PSer/HA MP scaffolds promote hMSC differentiation. (A) Photographic (Right) and SEM (Left) images of BPLP-PSer/HA MP scaffolds. (Scale bars: Right, 5 mm; Left, 100 μ m.) (B) Intracellular ATP levels (normalized to DNA) of hMSCs cultured on different MPs in GM for 4 d. $n \geq 8$ biological replicates per group. (C and D) ALP production of hMSCs in GM without osteogenic inducers cultured on MPs in Transwell 3D models (C) and differentiated in OG medium for 21 d (D). $n = 3$ –5 biological replicates per group. (E) Compressive strength of round disk-shaped cell-MP constructs after cells differentiated for 1, 2, or 3 wk in OG medium. $n = 3$ cell-MP constructs per time point. All data are presented as mean \pm SD; * $P < 0.05$. (F) Photographic and fluorescent images of hMSC-MP constructs obtained with 21 d of culture in round Transwells (Left) or from in PDMS wells with permeable bottoms cast from 3D-printed letter molds in the shape of the letters P, S, and U (Right). (Scale bars: 5 mm.) (G) SEM images of the thick cell layer covering and bridging MPs (Upper) and the extensive interwoven ECM network (Lower Left) produced by hMSCs differentiated for 21 d in OG medium to enable mineral formation (Lower Right). (H) Fluorescent images (blue, green, and red channels) (Upper Left, Upper Right, and Lower Left, respectively) and H&E staining (Lower Right) of the cell-MP construct sections obtained by cryo-sectioning. (Scale bar: 1 mm.)

S8C) along with extensive ECM production forming intertwined networks that was accompanied by significant calcium phosphate mineral deposition (Fig. 5G and SI Appendix, Fig. S8D). Further, cryosectioning and H&E staining of the rounded bone-like disks revealed a homogeneous distribution of cells throughout the constructs (Fig. 5H) so that cells and MP interfaces were closely integrated (SI Appendix, Fig. S8E). Meanwhile, fluorescent imaging of the sections showed strong fluorescence from MPs at different excitation wavelengths, which also confirmed a highly porous framework generated by packed MPs in the Transwell (Fig. 5H) that was beneficial for cell interaction and tissue penetration.

Efficacy of BPLP-PSer/HA MPs in the Femoral Condyle-Defect Model. Next, to evaluate in vivo efficacy in promoting bone regeneration, we implanted BPLP-PSer/HA MPs into a rat femoral-condyle

femoral condyle-defect model, so that our MPs can bridge nonunion defects of endochondral origin even in the absence of exogenous cell sources and growth factors. Still, defect size and location are major determinants that affect the innate capacity for bone healing (28). In particular, craniofacial bone of intramembranous origin suffers from reduced healing responses due to a poor blood supply and relative deficiency of bone marrow sources (29, 30). Therefore, we performed a second *in vivo* study to evaluate the potential application of BPLP-PSer/HA MPs in rat critical-sized full-thickness cranial defects, considered a severe test for bone implants.

Quantitative micro-CT analysis of BMD revealed the superior *in vivo* performance of BPLP-PSer/HA over other groups. Meanwhile, histomorphometric analysis at 3 mo showed more woven bone (*SI Appendix, Fig. S10A*) and increased red-stained mature bone generated in the BPLP-PSer/HA group than in other groups (*Fig. 6E*). In contrast, the negative control defects were filled with loose fibrous connective tissue (*SI Appendix, Fig. S10B*). Immunohistochemical staining consistently revealed remarkably higher VEGF expression in peri-implant cells on BPLP-PSer/HA MPs than on MPs in the control groups (*Fig. 6E*), suggesting higher blood vessel-forming activity since VEGF-producing cells in bone could largely stimulate the formation of new blood vessels. More new blood vessels were found in the BPLP-PSer/HA group, especially at 1 mo (*Fig. 6F* and *SI Appendix, Fig. S10C*), with the presence of red blood cells indicating the vessels' functional connection to the surrounding circulation. Also, osteocalcin (OCN) staining revealed notably higher bone matrix-formation activity in peri-implant cells around BPLP-PSer/HA MPs. Collectively, both the femoral-condyle and the cranial-defect models confirmed that BPLP-PSer/HA MPs elicited faster and superior bone formation and osteointegration in defects; new bone formation and maturation found along the material surface indicated the extensive influence of the concerted action of citrate and PSer in fueling bone regeneration.

Discussion

The impressive *in vivo* performances of existing citrate-presenting materials in bone regeneration, demonstrated through numerous animal models (12, 13, 31–33), motivated us to investigate the biological mechanism of citrate action on bone development. The present study has identified citrate as an osteopromotive factor; specifically, its beneficial effects are mediated by SLC13a5, the plasma membrane transporter responsible for citrate uptake. Although citrate uptake has known to regulate cell energy homeostasis (17, 34), the link between the role of extracellular citrate in osteoblast metabolism and its eventual role in osteogenic differentiation has remained elusive. Here, we identify metabonegenic regulation, a previously unexplored central link in which citrate uptake mediates the metabolic regulation of cellular energy status that influences the osteophenotype progression of hMSCs, as the central mechanism underlying citrate-promoted osteodifferentiation.

Our findings support the involvement of SLC13a5 in the beneficial effects of citrate. We demonstrated the expression of SLC13a5 in hMSCs, further showing that citrate-elevated ALP expression was dependent on SLC13a5. These findings have significant implications in bone stem cell biology, providing a biological mechanism underlying the reported contribution of exogenous citrate in teeth and bone showing that SLC13a5 deficiency in mice leads to impaired bone formation and defective tooth development (35). Similarly, consumption of extracellular citrate has been found in cancer cells that are known to be metabolically active to meet their high energetic and synthetic needs. For example, the uptake of citrate from extracellular space is required by prostate cancer cells to support their advanced metastatic behavior (36). SLC13a5 inhibition in hepatocarcinoma cells has resulted in decreased ATP production and suppressed mTOR activity (34), leading to inhibited cell

proliferation. Our studies further demonstrated that inhibition of SLC13a5 in hMSCs negated the citrate-mediated metabolic changes such as ATP production, highlighting the metabolic impact of citrate on bone growth. In fact, any factor that diminishes cell energy production, whether through inhibiting the uptake of glucose, glutamine (4, 5), or citrate, as demonstrated in the present study, restricting oxygen for oxidative respiration (3), or decreasing the direct substrate for ATP synthesis (e.g., inorganic phosphate) (37), may impair bone formation by inhibiting energy-consuming activities. Given that serum and bone citrate has recently been found to be markedly reduced in aged and osteoporotic patients (38) and that potassium citrate supplementation, previously considered a buffering agent for diet acid loads, sustainably improves bone mass and density, the possibility that systemically administered citrate could contribute to elevated bone energy status and thus be a potential therapeutic method in bone diseases is worthy of further investigation.

Next, the expression pattern of SLC13a5 matched the stage-dependent effects of citrate supplementation (*Fig. 3B*), suggesting that hMSCs exhibit a higher demand for exogenous citrate during pre- and early-stage differentiation (toward Runx2 expression, protein synthesis, and so forth) when their primary energy production is via glycolysis, typically without the production of large amounts of endogenous citrate. In contrast, cell metabolism gradually shifts to oxidative phosphorylation in the later stages of osteodifferentiation, generating endogenous citrate via the TCA cycle (18, 38, 39) while binding exogenous citrate via the extracellular calcium nodules; together, these processes may account for the decreased influence of exogenous citrate on late-stage cell energy metabolism and eventually on osteodifferentiation. The metabonegenic mechanism may be worthy of future study to explore whether nutrient- or energy-sensing pathways (e.g., the mTOR and the AMPK pathways) are involved in citrate metabonegenic regulation, especially since citrate uptake increased mTOR-dependent protein synthesis and diminished the hypothalamic AMPK activity following exogenous supplementation (40). Moreover, the involvement and up-regulation of SLC13a5 rather than SLC16a1 as the lactate membrane transporter during active bone formation (10, 11, 41) highlights the advantages of citrate-based materials for orthopedic applications compared with traditional PLA-based materials.

The above findings not only contribute to a comprehensive understanding of the temporal dependence of exogenous citrate in coordinated bone formation but also provide guidance for designing materials to further improve citrate metabonegenic regulation. For example, the present study showed that the introduction of PSer as a natural organic phosphate donor uniquely complemented the metabonegenic effect of citrate, resulting in elevated intracellular ATP levels particularly in the later stages of hMSC differentiation and thus prolonging active osteogenesis. Consistently, BPLP-PSer also induced elevated ALP production in late-stage differentiating hMSCs, likely due to bioactive inorganic phosphates generated by both the incorporated PSer in the polymer (*SI Appendix, Fig. S3E*) and the soluble PSer released during degradation (*SI Appendix, Fig. S3D*). Of note, phosphate is known to enter hMSCs via a phosphate transporter to fuel osteogenesis (37) by serving as the primary substrate of F1F0-ATPase for ATP synthesis (21), which probably accounts for the proposed concerted citrate/PSer regulation of cell energy metabolism toward active osteophenotype progression, as depicted in *Fig. 1*. Although the primary degradation mechanism of BPLP family has been identified as a return to monomeric materials (15), soluble oligomers are also detected in the entire pool of degradation product. The PSer moiety in those oligomeric degradation products may be as effective as the soluble PSer due to the ability of ALP to release bioactive phosphate from both soluble (22) and chemically bound PSer (23), while the chemically bound citrate moiety might not be able

to participate in the metabonegenic processes (*SI Appendix, Fig. S2E*). Therefore, future study is required to identify each component in the degradation product pool and to understand how those oligomeric degradation products could affect osteodifferentiation, so as to obtain a full understanding of the collective regulatory role of BPLP-PSer degradation products on stem cells.

In the succession of studies described above, we designed BPLP-PSer/HA composite MP scaffolds to provide growth guidance and osteogenic benefits for accelerated bone repair. As a demonstrated scaffold modality, MP scaffolds provide abundant bioactive surfaces for cell interactions along with well-interconnected pores for fast tissue penetration (42), enabling in vitro 3D culture studies and facile in vivo applications for bone-defect filling or augmentation. More importantly, the resulting MP scaffolds are expected to provide a biomimetic citrate- (12, 13) and PSer-rich (*SI Appendix, Fig. S3D*) microenvironment for surrounding hMSCs during degradation. As expected, the incorporation of citrate greatly boosted cellular energy levels (Fig. 5B), and the further introduction of PSer led to sustained osteogenic activity of the surrounding osteoblasts (Fig. 5C and D). This is in accordance with our in vivo results showing that significantly more new and mature bone was formed by peri-implant cells around the BPLP-PSer/HA implants in animal models of different origin, since the activity of bone-forming cells is known to greatly affect the rate and extent of bone formation (43). Of note, VEGF expression was highest on peri-implant cells surrounding the BPLP-PSer/HA implants and was accompanied by greater numbers of new blood vessels. Since extracellular citrate is known to promote angiogenesis (44), a possible synergy between PSer and citrate toward angiogenesis awaits further investigation. Moreover, BPLP-PSer represents a singular base material that can be readily tuned to match the temporal needs of osteopromotive factors at different stages of bone healing, either by optimizing material degradation for soluble citrate/PSer release or by incorporating other microenvironment factors (e.g., cells or biochemical or biophysical factors) that can coordinate with citrate metabonegenic regulation to amplify bone regrowth.

In conclusion, in this work we have attained an understanding of the effect of citrate on osteophenotype progression, revealing a previously unexplored expression pattern of the SLC13a5 citrate transporter during osteodifferentiation and a mechanism focusing on the metabolic regulation of citrate to elevate cell energy status for bone formation (i.e., citrate metabonegenic regulation). These findings not only identify citrate as a metabolic factor that is favorable for osteodifferentiation in the stem cell microenvironment but also suggest that the use of citrate should be considered in bone biomaterials design. The biomimetic BPLP-PSer/HA provided a prolonged citrate-mediated metabonegenic effect well into the late stages of differentiation, demonstrating therapeutic potential for bone injuries and particularly for bone-defect filling or augmentation. In addition to its benefits in osteodifferentiation, and because the role of cross-talk between cell metabolism and the regulation of differentiation (45), especially in stem cells and immune cells, has been increasingly appreciated, materials-mediated metabolic regulation provides a unique opportunity for the further investigation of unexplored questions. For example, could materials-derived or exogenous supplemented citrate also contribute to the regulation of other differentiation processes with high metabolic demands, such as cardiogenesis or neurogenesis? Therefore, our present finding that citrate is a central link bridging the building blocks of materials with the metabolic events in cells may have broader implications in a wide range of tissue-engineering scenarios, opening avenues in stem cell biology and future biomaterials design.

Materials and Methods

hMSC Culture and Differentiation Study. hMSCs with more than six passages were used in the present differentiation study. To assess the effect of citrate on osteogenic differentiation, cells at ~80% confluence were treated with an established OG medium (low-glucose DMEM with 10^{-7} M dexamethasone, 0.05 mM ascorbate-2-phosphate, and 0.01 M β -glycerophosphate) supplemented with citrate (pH adjusted) at different concentrations between 20 μ M and 2,000 μ M to initiate differentiation and were cultured for a predetermined number of days. The differentiation study procedure is described in detail in *SI Appendix, Supplementary Materials and Methods*.

Protein Synthesis, ATP Measurements, and OCR and Extracellular Acidification Rate Measurements. To assess the effects of citrate on protein synthesis, undifferentiated hMSCs seeded in 96-well black-walled plates were treated with growth medium supplemented with 200 μ M of citrate, Chx or Torin 1, or both. After 24 or 96 h of incubation, protein synthesis was measured using the Protein Synthesis Assay Kit (Cayman Chemical). For intracellular ATP, mitochondria respiration, and glycolytic flux studies, hMSCs and differentiating hMSCs (differentiated for 14 d) were cultured in 96-well black-walled plates with/without citrate supplementation before measurement with the Luminescent ATP Detection Assay Kit (Abcam), the Extracellular O_2 Consumption Assay (Abcam), or the Glycolysis Assay Kit (Abcam), respectively. To inhibit citrate uptake, cells were pretreated for 1 h with 2 μ M PF06761281 (Sigma-Aldrich) (the inhibitor for SLC13a5) before the medium supplemented with both citrate and PF06761281 was added to the cells.

Synthesis, Characterization, and Properties of BPLP-PSer. For BPLP-PSer-0.2 synthesis, citric acid, 1,8-octanediol, and O-phospho-DL-serine at molar ratios of 1:1.2:0.2 were mixed in a round-bottomed flask. After melting at 160 °C for 20 min, the temperature was lowered to 140 °C, and the mixture was stirred continuously for another 50 min with the stirring speed lowered gradually from 800 rpm to 80 rpm to produce the BPLP-PSer prepolymer. The prepolymer was then dissolved in 1,4-dioxane and purified by precipitation in water, followed by freeze-drying and storage in brown bottles at -20 °C. The yield of BPLP-PSer synthesis is ~86%. Next, the PSer incorporation was characterized by 31 P NMR analysis and HPLC (Shimadzu). The procedure is described in detail in *SI Appendix, Supplementary Materials and Methods*.

Preparation and Characterization of the MP Scaffold. To prepare polymer/HA microparticulate scaffolds, 1.25 g of prepolymer was first dissolved in 1,4-dioxane to prepare 30% (by weight) polymer solutions followed by mixing with 1.25 g of HA (purum p.a. $\geq 90\%$; Sigma-Aldrich) and 10 g of NaCl particles with diameters of 150–250 μ m. The mixture was spread on Teflon dishes until clay-like to form thin film scaffolds. After solvent evaporation, the scaffolds were cross-linked at 80 °C for 3 d, and all salts were leached by soaking the scaffolds in water. After freeze-drying, the prepared porous scaffolds were ground and sieved to collect the MPs with sizes between 250–425 μ m.

hMSC Differentiation with MP Scaffolds. To evaluate hMSC differentiation on MPs, 25 mg of MPs were sterilized and transferred into Transwell inserts (Sigma-Aldrich) placed in 24-well plates. Then hMSCs at densities of 1.3×10^5 cells per insert were seeded and mixed with MPs. After culturing in GM medium for 14 and 21 d or in OG medium for 14 and 21 d, the generated round disk-like cell-MP constructs were washed thoroughly with PBS. One portion of the constructs was lysed with RIPA buffer to generate cell lysate and was subjected to further ALP assay and DNA quantification; the other portion was carefully removed from the inserts so that photographs could be taken and their compressive mechanical properties tested or so they could be fixed with 4% paraformaldehyde for cryo-sectioning at a thickness of 25 μ m followed by H&E staining and observation under a microscope.

Rat Critical-Sized Femoral Condyle and Cranial Defects. Sprague-Dawley rats (male, age 8–10 wk, weighing ~300 g) were used for in vivo evaluation of our microparticles. All animal experiments were carried out in compliance with a protocol approved by Southern Medical University's Animal Care and Use Committee. The animals were randomly divided into four groups in which (i) defects were filled with BPLP-PSer/HA microparticles (BPLP-PSer/HA group); (ii) defects were filled with POC/HA microparticles (POC/HA group); (iii) defects were filled with PLGA/HA microparticles (PLGA/HA group); and (iv) defects were left empty as a negative control (control group). Bone defects with a diameter of 3.5 mm were drilled at both sides of lateral femoral condyles, and pit defects 5 mm in diameter were made in the skull to create critical-sized femoral condyle and cranial defect models, respectively.

The implants, after being wetted with sterile saline, were inserted into defects via press fit. After all surgical procedures, the rats were kept in cages and maintained with a regular laboratory diet. The knees and skulls were harvested after 1, 2, and 3 mo of implantation for micro-CT and histological analysis. Detailed procedures are provided in *SI Appendix, Supplementary Materials and Methods*.

Statistical Analysis. All quantitative data are presented as mean \pm SD with a minimum of three independent samples. Statistical analyses were performed

using Statistical Package for Social Sciences (SPSS; v.18) software, and ordinary one-way ANOVA was performed on three or more groups with the Tukey post hoc test applied within groups. A two-tailed unpaired *t* test was applied when only two groups were compared. *P* values < 0.05 were regarded as statistically significant.

ACKNOWLEDGMENTS. This work was supported in part by NIH Grants CA182670, EB024829, and AR072731, Cystic Fibrosis Foundation Research Grant YW17G0, and National Natural Sciences Foundation of China Grant 31529002.

1. Laurencin C, Khan Y, El-Amin SF (2006) Bone graft substitutes. *Expert Rev Med Devices* 3:49–57.
2. Lane SW, Williams DA, Watt FM (2014) Modulating the stem cell niche for tissue regeneration. *Nat Biotechnol* 32:795–803.
3. Wise DR, et al. (2011) Hypoxia promotes isocitrate dehydrogenase-dependent carboxylation of α -ketoglutarate to citrate to support cell growth and viability. *Proc Natl Acad Sci USA* 108:19611–19616.
4. Wei J, et al. (2015) Glucose uptake and Runx2 synergize to orchestrate osteoblast differentiation and bone formation. *Cell* 161:1576–1591.
5. Karner CM, Esen E, Okunade AL, Patterson BW, Long F (2015) Increased glutamine catabolism mediates bone anabolism in response to WNT signaling. *J Clin Invest* 125:551–562.
6. Mycielska ME, Milenkovic VM, Wetzel CH, Rümmele P, Geissler EK (2015) Extracellular citrate in health and disease. *Curr Mol Med* 15:884–891.
7. Iacobazzi V, Infantino V (2014) Citrate—New functions for an old metabolite. *Biol Chem* 395:387–399.
8. Rives ML, Shaw M, Zhu B, Hinke SA, Wickenden AD (2016) State-dependent allosteric inhibition of the human SLC13A5 citrate transporter by hydroxysuccinic acids, PF-06649298 and PF-06761281. *Mol Pharmacol* 90:766–774.
9. Dickens F (1941) The citric acid content of animal tissues, with reference to its occurrence in bone and tumour. *Biochem J* 35:1011–1023.
10. Thalji G, Gretzer C, Cooper LF (2013) Comparative molecular assessment of early osseointegration in implant-adherent cells. *Bone* 52:444–453.
11. Mantila Roosa SM, Liu Y, Turner CH (2011) Gene expression patterns in bone following mechanical loading. *J Bone Miner Res* 26:100–112.
12. Tran RT, et al. (2014) Synthesis and characterization of biomimetic citrate-based biodegradable composites. *J Biomed Mater Res A* 102:2521–2532.
13. Xie D, et al. (2015) Development of injectable citrate-based bioadhesive bone implants. *J Mater Chem B Mater Biol Med* 3:387–398.
14. Schneiders W, et al. (2007) Effect of modification of hydroxyapatite/collagen composites with sodium citrate, phosphoserine, phosphoserine/RGD-peptide and calcium carbonate on bone remodelling. *Bone* 40:1048–1059.
15. Yang J, et al. (2009) Development of aliphatic biodegradable photoluminescent polymers. *Proc Natl Acad Sci USA* 106:10086–10091.
16. Reinstorf A, et al. (2004) Phosphoserine—A convenient compound for modification of calcium phosphate bone cement collagen composites. *J Mater Sci Mater Med* 15:451–455.
17. Huard K, et al. (2015) Discovery and characterization of novel inhibitors of the sodium-coupled citrate transporter (NaCT or SLC13A5). *Sci Rep* 5:17391.
18. Pattappa G, Heywood HK, de Bruijn JD, Lee DA (2011) The metabolism of human mesenchymal stem cells during proliferation and differentiation. *J Cell Physiol* 226:2562–2570.
19. Ying X, et al. (2014) Phosphoserine promotes osteogenic differentiation of human adipose stromal cells through bone morphogenetic protein signalling. *Cell Biol Int* 38:309–317.
20. Park JW, Kim YJ, Jang JH, An CH (2011) MC3T3-E1 cell differentiation and in vivo bone formation induced by phosphoserine. *Biotechnol Lett* 33:1473–1480.
21. Bose S, French S, Evans FJ, Joubert F, Balaban RS (2003) Metabolic network control of oxidative phosphorylation: Multiple roles of inorganic phosphate. *J Biol Chem* 278:39155–39165.
22. Shinozaki T, Watanabe H, Arita S, Chigira M (1995) Amino acid phosphatase activity of alkaline phosphatase. A possible role of protein phosphatase. *Eur J Biochem* 227:367–371.
23. Spoerke ED, Anthony SG, Stupp SI (2009) Enzyme directed templating of artificial bone mineral. *Adv Mater* 21:425–430.
24. Xie Z, et al. (2017) Synthesis and characterization of citrate-based fluorescent small molecules and biodegradable polymers. *Acta Biomater* 50:361–369.
25. Hartgerink JD, Beniash E, Stupp SI (2001) Self-assembly and mineralization of peptide-amphiphile nanofibers. *Science* 294:1684–1688.
26. Puleo DA, Nanci A (1999) Understanding and controlling the bone-implant interface. *Biomaterials* 20:2311–2321.
27. Coathup MJ, Cai Q, Campion C, Buckland T, Blunn GW (2013) The effect of particle size on the osteointegration of injectable silicate-substituted calcium phosphate bone substitute materials. *J Biomed Mater Res B Appl Biomater* 101:902–910.
28. Fini M, et al. (2005) The healing of confined critical size cancellous defects in the presence of silk fibroin hydrogel. *Biomaterials* 26:3527–3536.
29. Dupoirieux L, Pourquier D, Picot MC, Neves M (2001) Comparative study of three different membranes for guided bone regeneration of rat cranial defects. *Int J Oral Maxillofac Surg* 30:58–62.
30. Spicer PP, et al. (2012) Evaluation of bone regeneration using the rat critical size calvarial defect. *Nat Protoc* 7:1918–1929.
31. Sun D, et al. (2014) Citric acid-based hydroxyapatite composite scaffolds enhance calvarial regeneration. *Sci Rep* 4:6912.
32. Tang J, et al. (2015) Fast degradable citrate-based bone scaffold promotes spinal fusion. *J Mater Chem B Mater Biol Med* 3:5569–5576.
33. Guo Y, et al. (2015) Citrate-based biphasic scaffolds for the repair of large segmental bone defects. *J Biomed Mater Res A* 103:772–781.
34. Li Z, et al. (2017) Silencing of solute carrier family 13 member 5 disrupts energy homeostasis and inhibits proliferation of human hepatocarcinoma cells. *J Biol Chem* 292:13890–13901.
35. Irizarry AR, et al. (2017) Defective enamel and bone development in sodium-dependent citrate transporter (NaCT) SLC13a5 deficient mice. *PLoS One* 12:e0175465.
36. Mycielska ME, et al. (2018) Extracellular citrate affects critical elements of cancer cell metabolism and supports cancer development in vivo. *Cancer Res* 78:2513–2523.
37. Shih Y-RV, et al. (2014) Calcium phosphate-bearing matrices induce osteogenic differentiation of stem cells through adenosine signaling. *Proc Natl Acad Sci USA* 111:990–995.
38. Chen H, et al. (2018) Bone and plasma citrate is reduced in osteoporosis. *Bone* 114:189–197.
39. Fu X, et al. (2018) Runx2/Osterix and zinc uptake synergize to orchestrate osteogenic differentiation and citrate containing bone apatite formation. *Adv Sci* 5:1700755.
40. Stoppa GR, et al. (2008) Intracerebroventricular injection of citrate inhibits hypothalamic AMPK and modulates feeding behavior and peripheral insulin signaling. *J Endocrinol* 198:157–168.
41. Ferraz EP, et al. (2017) Bioactive glass-based surfaces induce differential gene expression profiling of osteoblasts. *J Biomed Mater Res A* 105:419–423.
42. Lappalainen OP, et al. (2016) Micro-CT analysis of bone healing in rabbit calvarial critical-sized defects with solid bioactive glass, tricalcium phosphate granules or autogenous bone. *J Oral Maxillofac Res* 7:e4.
43. Caetano-Lopes J, Canhão H, Fonseca JE (2007) Osteoblasts and bone formation. *Acta Reumatol Port* 32:103–110.
44. Binu S, Soumya SJ, Sudhakaran PR (2013) Metabolite control of angiogenesis: Angiogenic effect of citrate. *J Physiol Biochem* 69:383–395.
45. Agathocleous M, Harris WA (2013) Metabolism in physiological cell proliferation and differentiation. *Trends Cell Biol* 23:484–492.

Supplementary Information

Supplementary Materials and Methods

Supplementary Figures

Fig. S1 Additional results of osteo-promotive effects of citrate

Fig. S2 Additional results of citrate metabonegenic regulation and concerted action between citrate and PSer

Fig. S3 Additional results of BPLP-PSer synthesis and characterization.

Fig. S4 *In vitro* mineralization tests on polymer films

Fig. S5 *In vitro* mineralization tests and mechanical properties of polymer/hydroxyapatite (HA) composites.

Fig. S6 Additional results of cytocompatibility evaluation of BPLP-PSer.

Fig. S7 Additional results of BPLP-PSer/HA MP scaffolds and stem cell studies

Fig. S8 Additional results of hMSC differentiation on MPs in transwell 3D model.

Fig. S9 Additional *in vivo* results in femoral condyle defects.

Fig. S10 Additional *in vivo* results in cranial defects.

Other Supplementary Materials:

Supplementary Movie 1 (.MP4 format). Continuous pressing and recovery of hydrated and intact bone-like cell-Microparticule constructs shown in **Fig. 5F** & SI Appendix, **Fig. S8A**.

Supplementary Materials and Methods

Cell Culture and Medium

Human mesenchymal stem cells (hMSCs; Lonza) were cultured in low glucose Dulbecco's Modified Eagle Medium (DMEM) with 10 vol. % fetal bovine serum (FBS) (Atlanta Biologicals; Flowery Branch, GA) and GlutaMAX (Gibco Laboratories, Gaithersburg, MD). Mouse 3T3 embryo fibroblasts and L929 fibroblasts were respectively cultured in DMEM with 10 vol. % FBS and Eagle's Minimum Essential Medium (MEM) with 10 vol. % FBS. Human acute monocytic leukemia cells, THP-1, were thawed using RPMI-1640 with 20 vol. % FBS and 0.05 mM 2-Mercaptoethanol, with the culture flask placed upright for better cell recovery. After passaging cells once, the culture flask was laid down and cells were cultured in RPMI-1640 medium with 10 vol. % FBS and 0.05 mM 2-Mercaptoethanol. All the cells were cultured in a humidified atmosphere with 5% CO₂ at 37 °C.

hMSCs Differentiation Studies

To determine whether citrate could induce osteogenic differentiation, hMSCs were cultured in growth medium supplemented with citrate for predetermined time periods. To evaluate whether citrate pretreatment could promote subsequent osteogenic differentiation, hMSCs were treated with 200 μM of citrate supplementation in growth medium for 4 days before the culture medium was changed to OG medium without citrate addition, and cultured with cells for predetermined time periods. To identify differentiation stage specific effects, citrate was supplemented into OG medium at different stages of differentiation (day 0-day 4; day 4-day 14; day 14-day 21). To evaluate whether soluble PSer could have an impact on the citrate effect, hMSCs were treated with OG medium supplemented with 200 μM of citrate as well as PSer at different concentrations between 40 and 1000 μM, and incubated for predetermined time periods. For osteo-phenotype progression assessment, cells were lysed, and alkaline phosphatase (ALP) production was quantified by using p-nitrophenyl phosphate (PNPP) as its substrate. Alizarin Red was used to stain the calcium nodules formed by the differentiating cells, and the calcium content in the nodules was quantified by Calcium Assay Kit (Sigma-Aldrich, St. Louis, MO) and normalized to protein amount as determined by BCA protein assay kit (Thermo ScientificTM, Waltham, MA). Expression of osteogenic master transcription factor Runx2 was examined by real-time PCR and by using a Runx2 ELISA kit (American Research Products, Inc.TM, Waltham, MA) according to manufacturer's instructions. Moreover, the expression of bone matrix proteins Collagen type I and osteopontin (OPN) were evaluated with real-time PCR, while OPN expression were also observed by immunofluorescent staining. Western blot was performed to evaluate the expression of ALP, OPN and SLC13a5 before or after differentiating for predetermined time periods.

ALP assay and DNA quantification

For ALP expression analysis, cell samples were lysed using RIPA buffer, and the cell lysate was centrifuged to remove debris. Then ALP activity measurement was performed by utilizing p-nitrophenyl phosphate (PNPP) which is hydrolyzed by ALP into a yellow colored product. Briefly, the PNPP stock solution (1M) was diluted with ALP assay buffer at a ratio of 1:100, 50 μL of which was subsequently added to 50 μL of lysate sample. After 10-30 min of incubation at 37°C, the plates were measured at 405 nm on a plate reader (TECAN, Männedorf, Switzerland). The same cell lysate solutions were used to determine DNA amount via a PicoGreen dsDNA quantification kit (Invitrogen, Carlsbad, CA) according to the manufacturer's instructions.

Alizarin Red Staining and Calcium Quantification

For Alizarin Red staining, cell samples were fixed with 4% paraformaldehyde, and 40 mM Alizarin red solutions were used to stain calcium nodules for 30 min with gentle shaking. After thoroughly washing, the stained cells were observed on a Microscope (Nikon, Tokyo, Japan). For calcium quantification,

cell samples were washed with PBS and decalcified in 0.6 N HCl for 12 h with gentle shaking. Calcium content in the supernatants was determined colorimetrically by using the Calcium assay kit (Sigma-Aldrich, St. Louis, MO). Considering that the DNA level may be more susceptible to the acidic HCl solution, compared with the protein level, the protein content in cell lysate solutions (lysed with buffer containing 0.1N NaOH and 0.1% sodium dodecyl sulphate (SDS)) was selected to normalize calcium content, determined by using the Pierce BCA protein assay kit (Thermo Scientific™, Waltham, MA) according to manufacturer's instructions.

Real-time PCR

Total RNA from whole cells was isolated with QIAGEN RNeasy kit (Hilden, Germany) and was transcribed into cDNA using High-Capacity cDNA Reverse Transcription Kits (Applied Biosystems™, Foster City, CA). For quantitative analysis, real-time PCR was performed using cDNA as the template, together with TaqMan Gene Expression Master Mix and the TaqMan Gene Expression Assays with both primers and probe included (Applied Biosystems™, Foster City, CA), and using the ABI 7900HT Fast Real-Time PCR system (Applied Biosystems™, Foster City, CA) according to manufacturer's instructions. Human PPIA (Cyclophilin A) was used for normalization. The primers and TaqMan probe for human Runx2, Col1A1, SPP1 and PPIA were Hs00231692_m1, Hs00164004_m1, Hs00959010_m1, and Hs99999904_m1, respectively.

Immunofluorescent Staining

For OPN expression analysis, hMSCs differentiated for 21 days were fixed with 4% paraformaldehyde. After washing with PBS, cells were blocked using 0.1% PBST with 1%BSA/10% normal goat serum/0.3M glycerin at room temperature for 1 h. Then the rabbit anti-osteopontin primary antibody (Abcam; ab8448) 1: 500 diluted with blocking buffer was added to samples and incubated overnight at 4 °C. After washing with PBS 3 times, the samples were incubated with Alexa Fluro 647 labeled secondary antibody Goat-anti-rabbit IgG (Molecular Probes, Eugene, OR) 1:500 diluted with PBS-1%BSA for 1 h. Subsequently, DAPI 1:1000 diluted with PBS was applied to stain the cell nucleus, and the stained cells were observed and recorded on a Fluorescence microscope (Keyence BZ-9000, Osaka, Japan).

Western Blotting

To evaluate ALP, OPN and SLC13a5 expression, hMSCs differentiated in OG for predetermined days with different concentrations of citrate were lysed using ice-cold RIPA buffer with protease inhibitor added, and centrifuged at 16,000 g to remove insoluble debris. After protein quantification by BCA assay, gel electrophoresis was carried out on AnykD™ Mini-Protean TGX stain-free Protein gels at 50 V for 10 min, followed by 250 V for 10-20 min, and was transferred to PVDF membranes with the Trans-Blot Turbo™ system. Then, membranes were blocked with TBST-5 wt% non-fat milk at room temperature for 2 hr, and incubated with primary antibodies (anti-ALP & anti-OPN primary antibody: Abcam, Cambridge, UK; anti-SLC13a5 antibody: CUSABIO, TX, USA) overnight at 4°C. After washing with TBST with five times for 5 min, the membranes were incubated in the HRP conjugated secondary antibody solution diluted in TBST-5 wt% non-fat milk for 1 hr at room temperature, followed by rinsing and incubating with Clarity™ western ECL substrate mixture for 5 min, which was finally imaged by the ChemiDoc MP imager.

NMR and HPLC Determination of PSer

For ³¹P nuclear magnetic resonance (NMR) analysis, 5 mg of polymer was dissolved in 1 mL of deuterated dimethyl sulfoxide (DMSO-d₆; Sigma-Aldrich, St. Louis, MO) and the ³¹P-NMR was

recorded on a Bruker Advance 600 NMR spectrometer (Bruker, Billerica, MA). High performance liquid chromatography (HPLC; Shimadzu, Kyoto, Japan) was performed to confirm the presence of PSer in polymer degradation products and to quantify the PSer released from polymer films. To prepare degradation products, 0.5 g polymer films were fully degraded in 5 mL 0.2 N NaOH solution, and 2N HCl was added to adjust the pH to be 7.2-7.4. To determine the PSer concentration in the releasing media, films at the diameter of 16 mm were put in 24 well plates and 1 mL of PBS was added to each well. After 3, 7 and 14 days, the release media was collected for analysis. For HPLC determination, 220 μ L of each prepared samples were mixed with 100 μ L of 1.5M NaHCO₃ (pH 9.0) and 200 μ L of 2 mg/mL of dabsyl chloride in acetone followed by vortexing. After heating to 70°C for 10 min, the mix was subsequently dried under vacuum, followed by resuspending with 400 μ L of 70% ethanol and centrifuging for 2 min at 14,000g. Finally, the supernatant was transferred to a new tube and filtered through a 0.2 μ m filter. HPLC analysis was performed on a Shimadzu HPLC system equipped with a UV-visible PDA detector and a C18 column at room temperature. The detection of PSer was set at 460 nm, and a calibration curve of PSer was obtained under the same conditions.

Synthesis of CA-PSer

To synthesize the fluorescent small molecule CA-PSer, citric acid and PSer at molar ratio of 1:1 were first dissolved in 20 mL of DI water. The reaction was conducted at 140 °C stirred continuously with the stirring speed gradually lowered from 800 rpm to 80 rpm. Then, the reaction was terminated by adding cold DI water to dissolve the products, followed by freeze-drying.

Photoluminescent Properties of BPLP-PSer

The photoluminescent properties of polymers were studied using a Horiba FluoroMax-4 spectrofluorometer (Horiba Scientific, Edison, NJ). The fluorescent spectra was measured in 1,4-dioxane solutions at concentrations of 2 wt. % with excitation and emission slit sizes of 1.5 nm by 1.5 nm unless otherwise specified. The photostability of polymers and commercial small molecule were determined by monitoring the decay of the emission intensity at their maximum excitation and emission wavelengths under 3 h of continuous illumination in the spectrofluorometer.

Preparation of Polymer Films and Polymer/HA Composites

To prepare polymer films, the BPLP-PSer pre-polymer was dissolved in 1,4-dioxane to obtain a 30 wt. % solution and then was casted into a Teflon mold followed by solvent evaporation and thermal cross-linking at 80 °C for 3 days and 100 °C for another 3 days unless otherwise specified. To prepare BPLP-PSer/HA composites, 30 wt. % pre-polymer solution was mixed with 50 wt. % HA, and stirred in teflon dishes to prepare homogenous mixture. Following solvent evaporation, the composite mixture was rolled up and pressed into thin sheet using pasta roller machine, which was subsequently cut into round disks, and lastly cross-linked at 80 °C for 3 days.

Degradation Studies

For accelerated degradation studies, polymer films were cut into round disks weighing ~50 mg (d=10 mm; Thickness~0.5 mm) and placed in tubes containing 10 mL of 0.05 M NaOH solutions. All samples were incubated at 37 °C for predetermined times. At each time point, the samples were taken out, washed thoroughly with deionized water and subsequently lyophilized. Film degradation was measured by mass remaining according to equation 1:

$$W_1/W_0 \times 100\% \tag{1}$$

where W_0 refers to the original scaffold weight and W_1 represents the remaining film weight. The *in vitro* degradation of POC-PSer films was also monitored by fluorescent analysis. The remaining fluorescent signal in lyophilized films was measured on an *in vivo* fluorescent imaging system (Maestro™ EX, Woburn, MA) and the degradation was evaluated using equation 2:

$$F_1/F_0 \times 100\% \quad (2)$$

where F_0 refers to the fluorescence signal of the original film and F_1 represents that of the degraded film. In conjunction, fluorescent molecules released into degradation media was quantified by transferring 200 μL of the degradation media to 96 black well plates and by measuring on a plate reader (TECAN; Männedorf, Switzerland) at 370 nm excitation and 440 nm emission. The degradation pattern was plotted as cumulative release profile over the time using equation 3:

$$F_2/F_{\text{total}} \times 100\% \quad (3)$$

where F_{total} refers to the total fluorescence signal that released from polymer from and F_2 represents the cumulative released fluorescence signal at specific time point. All three curves were fit with Allometric2.

For degradation studies under neutral conditions, polymer films were cut into round disks weighing ~50 mg ($d=10$ mm; Thickness~0.5 mm) and placed in tubes containing 10 mL of PBS solutions ($\text{pH}=7.2-7.4$). All samples were incubated at 37 °C for predetermined times and PBS was changed every week. At each time point, the samples were taken out, washed thoroughly with deionized water and subsequently lyophilized. Film degradation was measured by mass remaining according to equation 1.

***In vitro* Mineralization study and Scanning Electron Microscopy (SEM) Observation**

To evaluate the bioactivity of polymer surfaces, polymer films and composite disks with diameters of 6 mm were incubated at 37 °C in simulated body fluid (5 \times mSBF) modified based on a method described elsewhere (1) for predetermined time periods before the films were washed thoroughly and air-dried. Finally, minerals formed on films/disks were finally observed and analyzed using FESEM (Zeiss Sigma) equipped with energy dispersive X-ray spectroscopy (EDS) elemental analysis after sputter coating with iridium (Emitec Sputter-Coater). Elemental data was collected at each area of interest at 10 kV and analyzed using AZtec (Oxford Instruments, Abingdon, UK).

Cytocompatibility Evaluation and hMSC Differentiation

Cytotoxicity Evaluation of Liquid Extraction of Polymer Films: To prepare liquid extracts of polymer films, both POC and BPLP-PSer films (thickness < 0.5 mm) were cut into round disks with diameters of 16 mm and placed into 12 well plates once sterilized. Next, 670 μL of complete culture medium was added and incubated with polymer films for 24 h at 37 °C with agitation. Next, the liquid extracts of different polymers were collected and added to L929 cells at sub-confluence in 96 well plates and incubated for 24 h before cell viability was measured with a CCK-8 assay (Dojindo Molecular Technologies Inc., Rockville, MD) according to international standard ISO 10993-5:2009(E).

Cytotoxicity Evaluation by Direct Contact: To evaluate the cytotoxicity of polymer films to 3T3 cells by direct contact, cells were seeded onto sterilized polymer films ($d=6$ mm) placed in 96 well plates and cultured for 24 h before the cell viability was evaluated with CCK-8 assay according to manufacturer's instructions.

Cytotoxicity Evaluation of Degradation Products: To prepare degradation products, 0.5 g polymer films were fully degraded in 5 mL 0.2 N NaOH solution, and 2N HCl was added to adjust the pH to be 7.2-7.4. Once centrifuged, the supernatant was filtered to another tube. Dilutions of degradation products were prepared using culture medium and 20 μL of each dilution were added to cells cultured in 96 well plates with 200 μL medium. After culturing for 24 h, CCK-8 evaluation (Dojindo, Rockville, MD) was performed according to manufacturer's instructions.

Cell Proliferation Assay: To test cell proliferation on polymer films, BPLP films with different feeding ratio of PSer (d = 6 mm) were sterilized and placed in 96 well plates before hMSC cells were seeded at densities of 10,000 cells/ cm² to each well and incubated on the films. After 1, 3 and 5 days, cell viability was evaluated with CCK-8 assay (Dojindo, Rockville, MD).

Immune Evaluation of Polymer Cytocompatibility: Immune evaluation of polymer films with THP-1 monocyte model cells was performed. Briefly, 700 μ L of THP-1 monocytes at densities of 10⁶ cells/mL were incubated with polymer film disks (PLA and BPLP-PSer) with the diameter of 10 mm in 48 well plates. As positive control, 50 ng of Lipopolysaccharides (LPS) from *Escherichia coli*0111:B4 (Sigma-Aldrich, St. Louis, MO) was added to THP-1 cell suspensions in wells without films to positively activate THP-1 to produce inflammatory factors. After 18 hours, the cell suspension of each sample was collected and centrifuged at 1500 rpm for 5 min. The supernatant was collected to determine the IL-1 β concentrations using ELISA kit (R&D systems, Minneapolis, MN) while the pelleted cells were resuspended by CCK-8 working solutions to evaluate their cell viability.

Mechanical Testing

Compression testing of cylindrical composites: To test the compressive strength of polymer/HA composites, cylindrical samples were first prepared by mixing pre-polymers with various amounts of HA particles to prepare composites of 50 wt. % and 60 wt. % HA. Once the polymer-HA mixtures became clay-like, they were then inserted into PTFE tubing molds followed by post-polymerizing at 80 °C for 3 days and then 100 °C for 3 days. Next, compression tests were performed on the cylindrical shaped specimens using an Instron 5966 machine equipped with a 10 kN load (Instron, Norwood, MA) at a rate of 1.3 mm/min to failure. The initial modulus was calculated by measuring the gradient at 10% of compression of the stress-strain curve.

Compression testing of hMSC-MPs constructs: To test the compressive strengths of cell-Mps, the constructs were differentiated for predetermined time in transwell, then were taken out of transwells carefully. Compression tests were then performed on the constructs on an Instron 5966 machine equipped with a 1 kN load (Instron, Norwood, MA) at a rate of 1.3 mm/min, with the test reaching completion when 50% of the original specimen height was reached. The initial modulus was calculated by measuring the gradient at 10% of compression of the stress-strain curve.

ALP Treatment of Polymer Films and Determination of Inorganic Phosphate

To determine whether ALP could cleave the phosphate group from polymer films, BPLP-PSer and POC films were cut into small disks (d=10 mm; Thickness~0.5 mm) and placed in 48 well plates (n=8). Next, 250 μ L/well of ALP solution in diethanolamine buffer with 5 U/mL of enzyme was added to each well and incubated from 30 min to 1 h before the samples were transferred to 1.5 mL tubes. Finally, the inorganic phosphate amount in each sample was determined by the PiPerTM Phosphate Assay Kit (P22061, Molecular Probes, Eugene, OR) according to the manufacturer's instruction.

hMSC Adhesion and Proliferation Study on MP Scaffold

To observe adhesion of hMSCs, 20 mg of BPLP-PSer/HA MPs were sterilized and transferred to a 5 mL centrifuge tube. Then, 2 mL of cell suspension solutions with 5 \times 10⁵ cells was added to the MPs in the tube followed by continuously mixing the two on a vertical sample mixer (ThermoFisher Scientific). Following every 1 h of shaking, the shaker was paused and the cap of the tube was opened to balance the culture medium. After 6 h of shaking, the cell suspension was removed, and the cells adhered onto MPs were washed twice with PBS, followed by fixed in 2.5% glutaraldehyde. After serial dehydration, critical-point drying and coating, the adherent cells on MPs were observed with SEM. For hMSC proliferation studies, 5-6 mg/ well of MPs were sterilized and transferred into 96 well plates.

Next, hMSCs at densities of 1.6×10^4 cells/cm² were seeded to each well. After 1, 3 and 7 days of culture, CCK-8 was performed to determine the cell viability according to the manufacturer's instruction.

hMSC Differentiation in "PSU" Shaped Molds

To obtain the "PSU" shaped cell-MPs constructs, the *in vitro* 3D culture models with permeable bottoms and with the shape of "P", "S" and "U" were prepared by making the three letters with PLA filaments by 3D printing, and by casting PDMS against the letters to fabricate letter-shaped penetrating cavities. Next, permeable membranes with pore sizes of 3 μ m were attached to the bottom of the cavity using nail polish, forming letter shaped wells which were prepared for cell culture by washing and sterilizing with 70% ethanol and UV exposure. Then, 80 mg of the sterilized MPs were seeded and mixed with 6.7×10^5 cells in each letter-culture model, which were cultured in GM for 24 h before changing to OG. After differentiating for 21 days, the generated cell-MPs constructs were taken out and fixed with 4% paraformaldehyde.

Rat Critical-sized Femoral Condyle Defect

To develop the critical-sized femoral condyle defects, the animals were anesthetized by intraperitoneal injection of chloral hydrate at a dosage of 0.4 mL/100g. A 1.5-2 cm medial incision on the lateral knee was created to expose the lateral femoral condyle. Bone defects with a diameter of 3.5 mm were drilled at both sides of lateral femoral condyles, which were constantly cooled with sterile saline. The implants, after being wetted with sterile saline, were next inserted into defects via press fit. After all surgical procedures, the rats were kept in cages and maintained with a regular laboratory diet. The knees were harvested after 1, 2 and 3 months of implantation for micro-CT analysis and histological analysis. Moreover, the tissue sections obtained from the BPLP-PSer/HA groups were subjected to fluorescent imaging.

Rat Critical Sized Cranial Defect

Surgeries were performed with animals under anesthesia induced by the intraperitoneal injection 0.4 mL/100 g of chloral hydrate. The surgical site was shaved and cleaned with a 70% ethanol solution. A subcutaneous injection of 0.5 mL of 1% lidocaine (local anesthetic) was given at the sagittal midline of the skull. Following this injection, a sagittal incision (1.5-2 cm long) was made over the scalp from the nasal bone to the middle sagittal crest, and the periosteum was bluntly dissected. A 5 mm diameter pit defect was made with a trephine drill, which was constantly cooled with sterile saline to prevent extensive heat damage. The calvarial disk was then carefully removed to avoid tearing of the dura, and implants were next inserted into defects via press fit. The periosteum and skin were completely closed by suturing with 6-0 vicryl, and the animals were monitored according to standard post-operative animal care protocols. Animals were ultimately anesthetized and sacrificed after 1, 2, 3 months post-surgery, and the skulls were collected for micro-CT imaging, histochemistry and immunostaining analysis.

Micro CT Analysis.

Bone formation within the fixed rat defects was evaluated via isolated bone mode using the LaTheta Laboratory X-ray CT scanning system LCT-200 (Hitachi Aloka Medical Ltd., Japan) at low voltage with an integration time of 200 ms for each of the 360 rotational steps. A total of 100 slices with resolutions of 96 μ m and voxel sizes of 48 μ m were collected, and the reconstructed dataset was segmented by an automated thresholding algorithm. The projection images were reconstructed into three-dimensional images using VGStudio MAX (version 2.2.2). The volume of interest (VOI) was defined as a hollow cylinder of a height that could cover the entire thickness of defect, and the bone

mineral density (BMD) among groups was calculated using Latheta software (Hitachi Aloka Medical Ltd., Japan).

Histological and Histomorphometric Analysis

Histological Analysis: The defect and surrounding tissues were fixed in 4% paraformaldehyde for 48 h, decalcified with 0.5 M ethylenediaminetetraacetic acid (EDTA) at pH 7.4 at 4 °C for 4-7 weeks, and embedded in paraffin. Tissues were sectioned with a 4- μ m thickness, deparaffinated with xylene, gradually hydrated, and stained with H&E for light microscopic analysis. Images were captured at 200 \times magnification using an Olympus B \times 51 microscope (Olympus, Japan) and a digital camera (ProgRes C14, Jenoptik, Germany).

Immunohistochemical Analysis: To detect osteocalcin (OCN) expression, paraffin-embedded sections were deparaffinated and dehydrated through a graded series of alcohol. Endogenous peroxidase activity was blocked with 3% hydrogen peroxide. Then, the sections were blocked with 5% normal goat serum for 1 h and incubated with the primary anti-OCN antibody (Abcam, Cambridge, MA; 1:50 dilution) at 4 °C overnight. The sections were washed with PBS three times and incubated with secondary HRP-Goat anti-mouse IgG (Proteintech Group, US) for 1 h at 37°C. Colorization was subsequently developed in DAB solution and counterstained by HE. Two individual pathologists assessed IHC staining in a blinded and randomized fashion.

Fluorescent Imaging of Tissue Sections. The paraffin embedded tissues were sectioned with 4-mm thickness, and the images of remnant scaffolds in those tissue sections were obtained using a BZ-9000 fluorescent microscope with a DAPI blue cube (EX 360/40) under the same exposure time. Then, the area of remaining scaffold and the integrated density reflecting the total fluorescence were analyzed using Image J.

Supplementary Figures

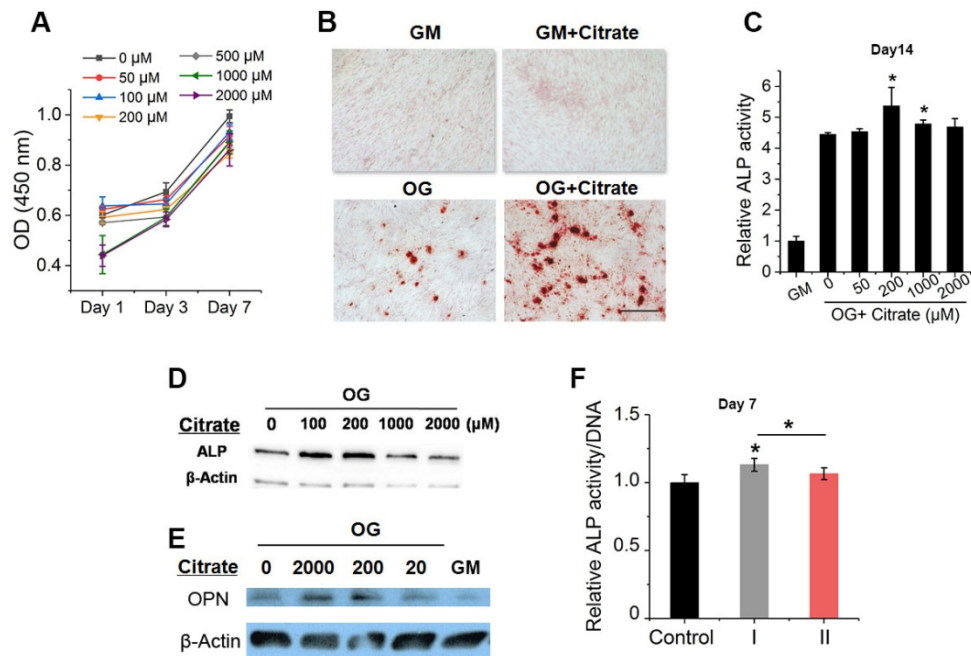


Fig. S1 Additional results of osteo-promotive effects of citrate. (A) Cell proliferation of hMSCs with treatment of citrate at different concentrations determined by cell counting kit-8 (CCK-8) assay ($n \geq 4$ biological replicates per group). (B) Calcium nodule formation by hMSCs cultured in growth medium (GM) or osteogenic medium (OG) with/without citrate supplementation at 200 μ M for 14 days. (C) Alkaline phosphatase (ALP) expression of differentiating hMSCs with citrate supplement in OG at different concentrations (0-2000 μ M) after 14 days of differentiation (Scale bar: 500 μ m). (D) ALP expression of hMSCs differentiated for 14 days in OG with citrate treatment at different concentrations (0-2000 μ M) by western blot. (E) Osteopontin (OPN) expression of hMSCs differentiated for 7 days in OG with citrate treatment at different concentrations (0-2000 μ M) by western blot. (F) ALP expression of differentiating hMSCs at day 7 with citrate supplemented in OG only at specific differentiation stages (In C&F, $n=3$ biological replicates; All plots represent mean \pm s.d.; * indicating $P < 0.05$).

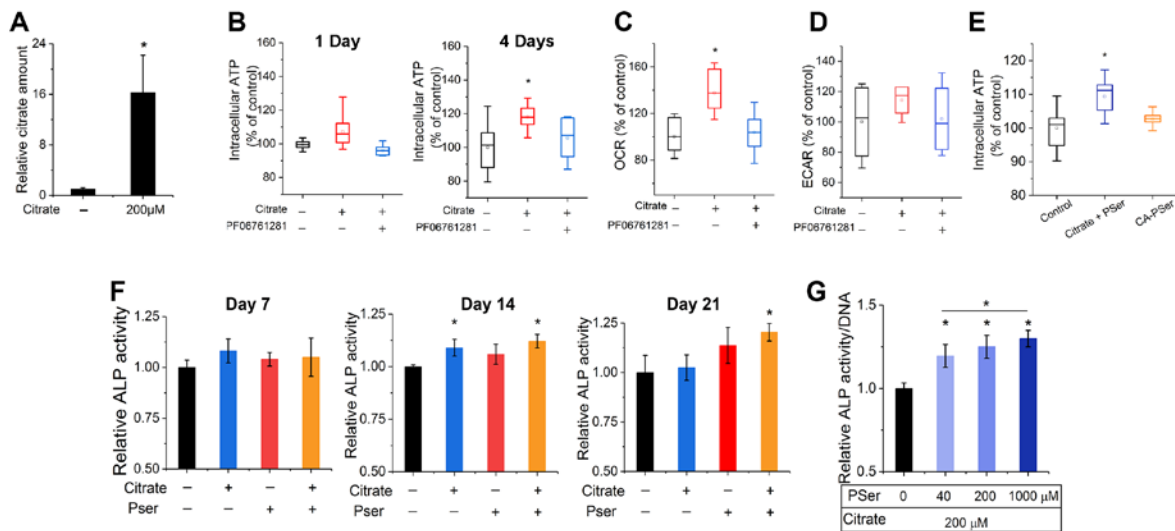


Fig. S2 Additional results of citrate metabonegenic regulation and concerted action between citrate and Pser. (A) Intracellular citrate amount in hMSCs incubated with/without citrate supplementation in GM for 24 h, determined by Citrate Assay (n=3 biological replicates per group). (B) Intracellular ATP determination of differentiating hMSCs (differentiated for 14 days) after 1 day (left) and 4 days (right) treatment of citrate, or citrate with SLC13a5 inhibitor PF06761281 in OG. (C) Oxygen consumption rate (OCR) study and (D) extracellular acidification rate (ECAR) study of differentiating hMSCs with 1 day treatment of citrate, or citrate with SLC13a5 inhibitor in OG. (E) Intracellular ATP determination of undifferentiated hMSCs after 1 day treatment of fluorescent small molecule CA-Pser (reacted by citric acid and Pser at molar ratio of 1:1) at 200 μ M, compared with the combination of soluble citrate (200 μ M) and Pser (200 μ M) diluted in DMEM. (In B-E, n \geq 6 biological replicates; All plots represent mean \pm s.d.; * indicating P<0.05). (F) ALP production of hMSCs with citrate, Pser or both supplemented in OG after 7, 14 and 21 days. (G) ALP production of hMSCs differentiated for 21 days with citrate and increasing concentrations of Pser (0-1000 μ M) supplement in OG. (In F&G, n \geq 4 biological replicates; All plots represent mean \pm s.d.; * indicating P<0.05).

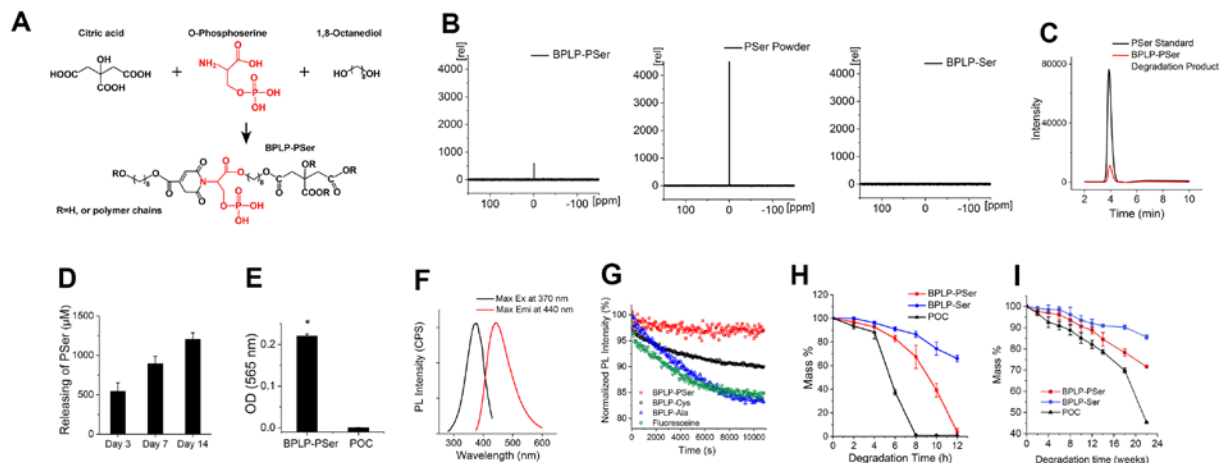


Figure S3 Additional results of BPLP-PSer synthesis and characterization. (A) Illustration of BPLP-PSer pre-polymer synthesis. (B) ^{31}P -nuclear magnetic resonance (NMR) spectra of BPLP-PSer pre-polymer solution (Left) showed a clear peak corresponding to that of the reference P-Ser sample (Middle), whereas the spectra of pre-BPLP-Ser (Right; P-Ser replaced with L-Ser in the reaction scheme above) lacked this peak. High performance liquid chromatography (HPLC) analysis further confirmed the presence of P-Ser (C) in the accelerated degradation products of BPLP-PSer films, as well as (D) in release medium incubated with BPLP-PSer films. (E) The inorganic phosphate that liberated by incubating ALP solution with different polymer films, determined by Piper phosphate assay. (F) Max excitation and emission of BPLP-PSer. (G) Photostability of BPLP-PSer. (H) Accelerated degradation in basic solution and (I) degradation in PBS under neutral pH of BPLP-PSer, BPLP-Ser, and POC films by measuring remaining weight, showing that the degradation of BPLP-PSer was slower than POC but faster than BPLP-Ser films (In D, E, H&I, $n \geq 5$ replicates per group; All plots represent mean \pm s.d.).

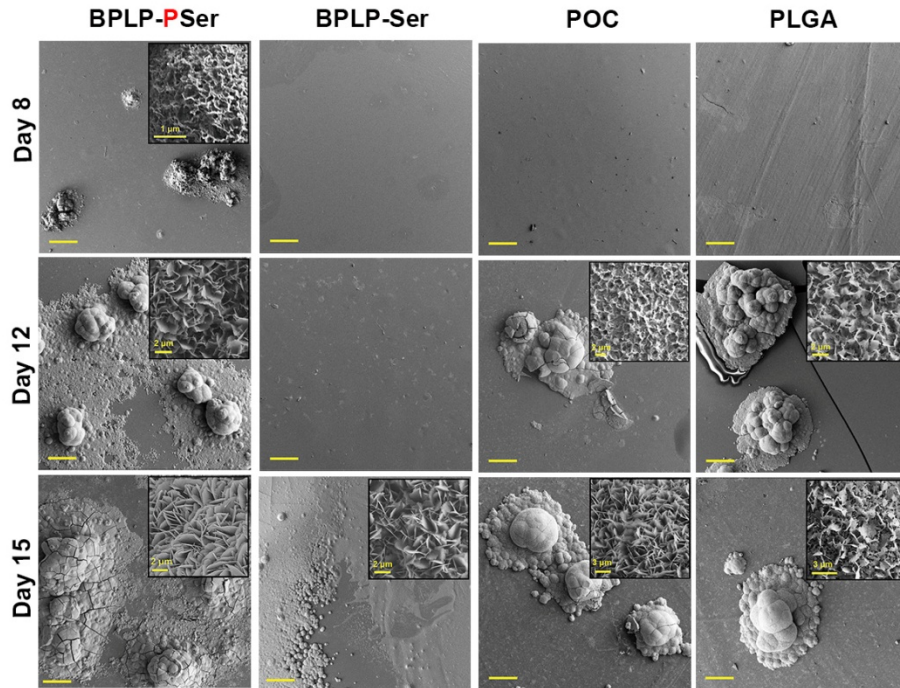


Figure S4 *In vitro* mineralization tests on polymer films (Scale bar: 200 μm). BPLP-PSer films induced accelerated mineral deposition compared to poly(octamethylene citrate) (POC) and BPLP-Ser as citrate-based materials control, as well as PLGA 75/25 as a general control. Inserted high magnification images presenting the morphology of the formed minerals further showed that BPLP-PSer films also induced earlier formation of petal-like minerals than other control materials, confirming the improved surface bioactivity brought by PSer incorporation.

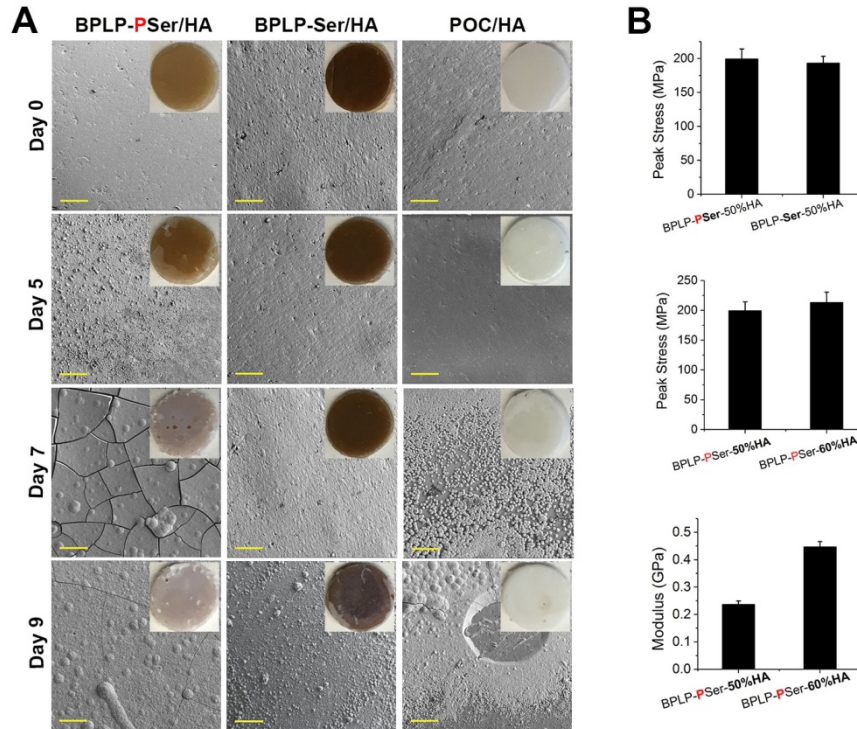


Figure S5 *In vitro* mineralization tests and mechanical properties of polymer/hydroxyapatite (HA) composites. (A) *In vitro* Mineralization test on polymer/HA composites showed an accelerated mineralization on BPLP-PSer/HA composites over control composites (Scale bar: 100 μ m). Inserted bright field images confirmed the superior performance of BPLP-PSer/HA. (B) Compressive mechanic properties of BPLP-PSer/50%HA, BPLP-PSer/60%HA and BPLP-Ser/50%HA cylindrical composites (n=6 composites per group; All plots represent mean \pm s.d.).

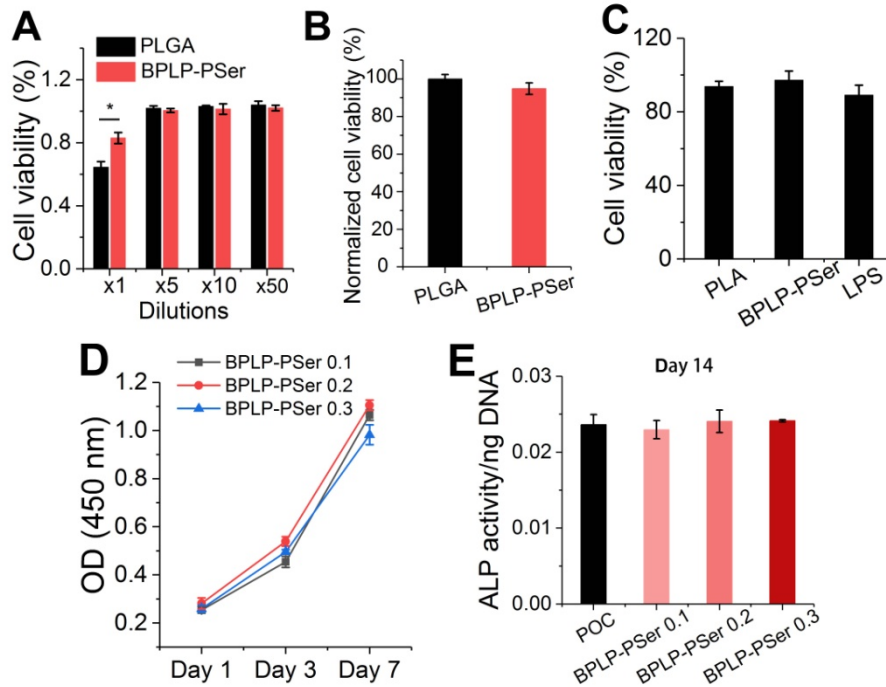


Figure S6 Additional results of cytocompatibility evaluations of BPLP-PSer. (A) Cytotoxicity of degradation products of polymer films to MG63 cells, showing reduced MG63 cytotoxicity compared to control PLGA75/25 samples. (B) Viability of MG63 cells cultured on polymer film with direct contact by CCK-8, showing no significant reduction of cell viability from culturing osteoblast-like MG63 cells directly on films (In A&B, n=6 biological replicates per group). (C) Cell viability of THP-1 cells incubated with polymer films tested by CCK-8, showing no negative effect on cell viability by incubating THP-1 with polymer films. (D) Cell proliferation on polymer films with various molar ratio of PSer incorporated determined by CCK-8. (E) ALP production of differentiating hMSCs cultured on polymer films in OG medium at day 14 (In C-E, n=3-4 biological replicates per group; All plots represent mean \pm s.d.; * indicating $P < 0.05$).

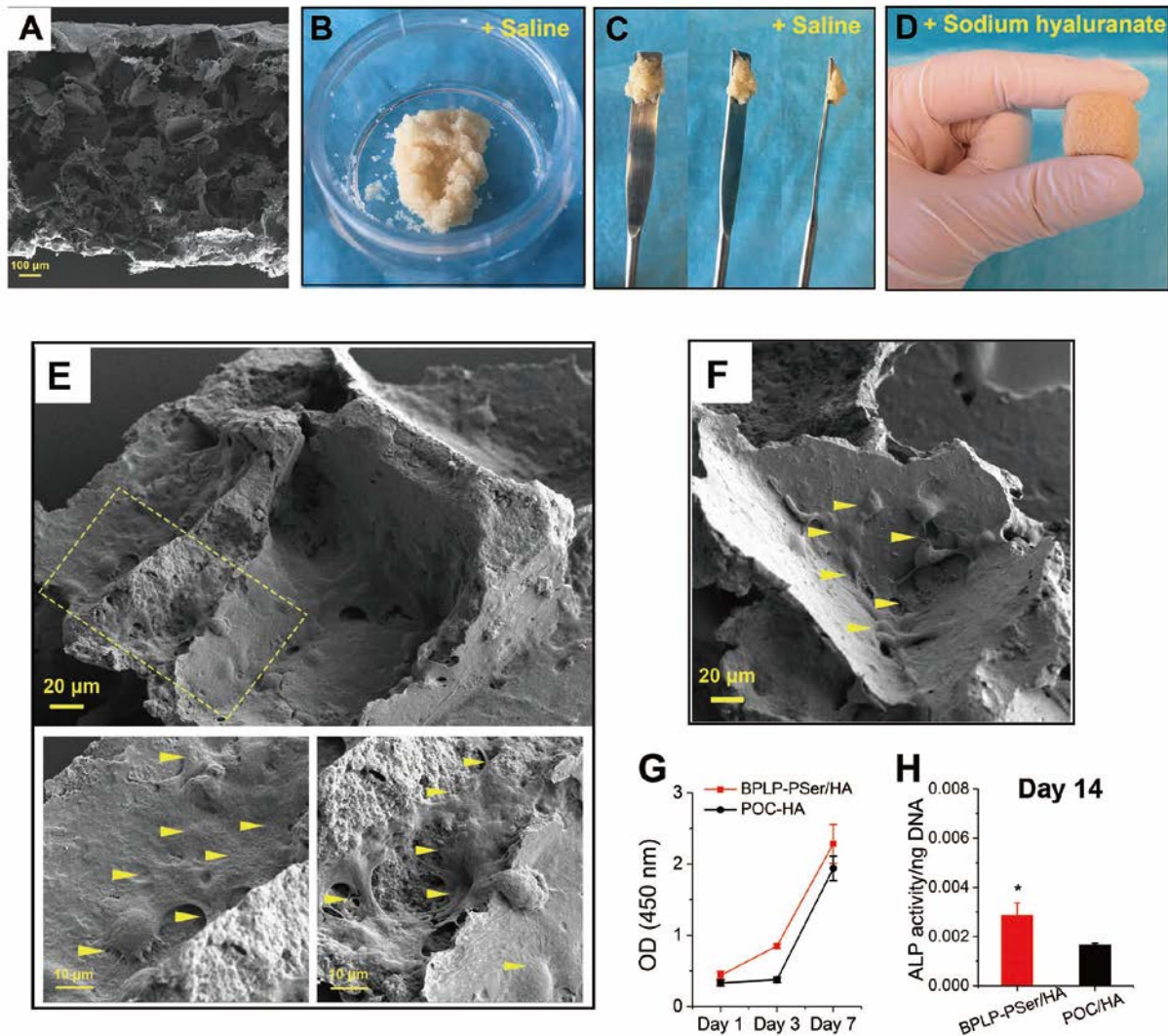


Figure S7 Additional results of BPLP-PSer/HA MP scaffolds and stem cell studies. (A) SEM image of the cross-section of BPLP-PSer/HA porous composite scaffold with pore sizes of ~150-250 μm prepared by salt-leaching method. (B) MP scaffolds wetted with sterilized saline (C) showing great handling capacity. (D) Moldability of BPLP-PSer MPs after mixed with 2 mg/mL of sodium hyaluronate solution. (E) SEM images of hMSCs adhered onto the "ridge and cliff" and (F) "groove" surface features of MP scaffolds after 6 h of dynamic seeding. (Arrow heads: adhered hMSCs) (G) Proliferation of hMSCs on different MP scaffolds tested by CCK8. (H) ALP production of hMSCs cultured on Mps in transwell 3D models in GM without osteogenic inducers at day 14 (In G&H, n=3-4 biological replicates per group; All plots represent mean \pm s.d.; * indicating $P < 0.05$).

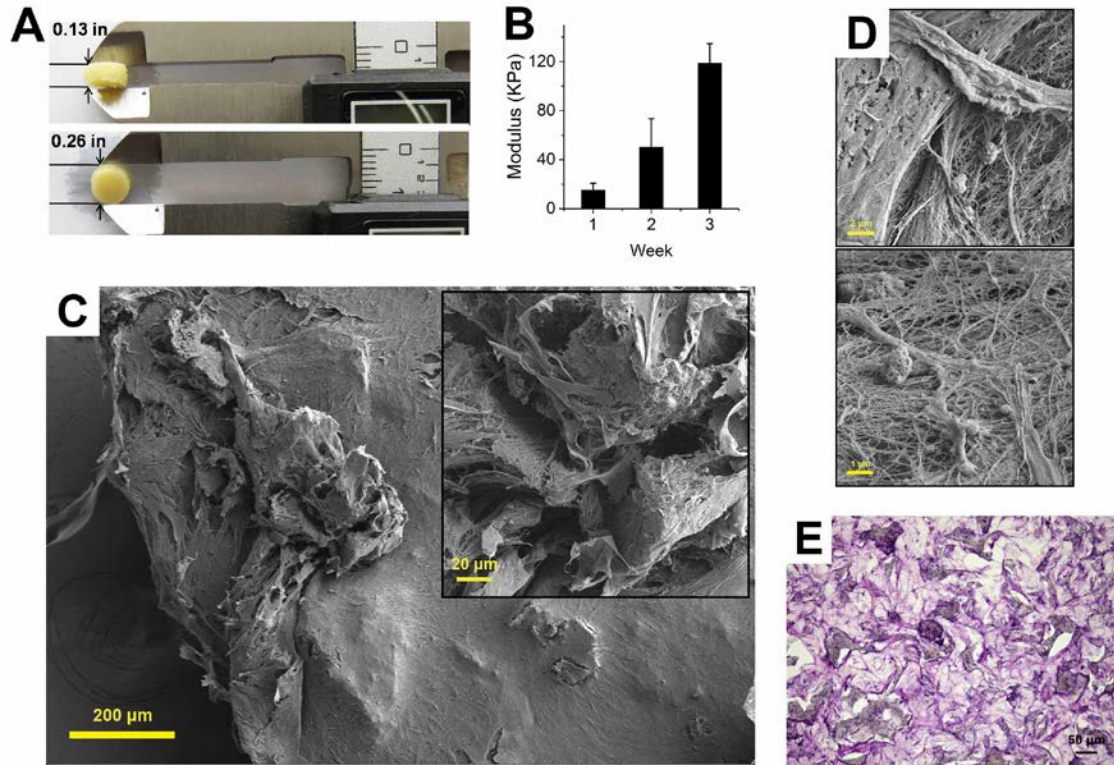


Figure S8 Additional results of hMSC differentiation on MPs in transwell 3D model. (A) Round disk shaped cell-Mps constructs with defined size capable of being prepared reproducibly by controlling the size of transwell, Mps amount and cell seeding density. (B) Compressive modulus of disk shaped cell-MP constructs after differentiating cells for 1, 2 and 3 weeks in OG (n=3 cell-MP constructs per time point). (C) Additional SEM images of a thick layer of differentiating hMSCs covering and bridging MP scaffolds to generate intact constructs. (D) Additional SEM images of massive extracellular matrix production produced by differentiating hMSCs with signs of minerals deposition. (E) H&E staining of the cryosections of cells-MP constructs showing the close and integrated interaction between cells and MPs (Scale bar: 50 μm).

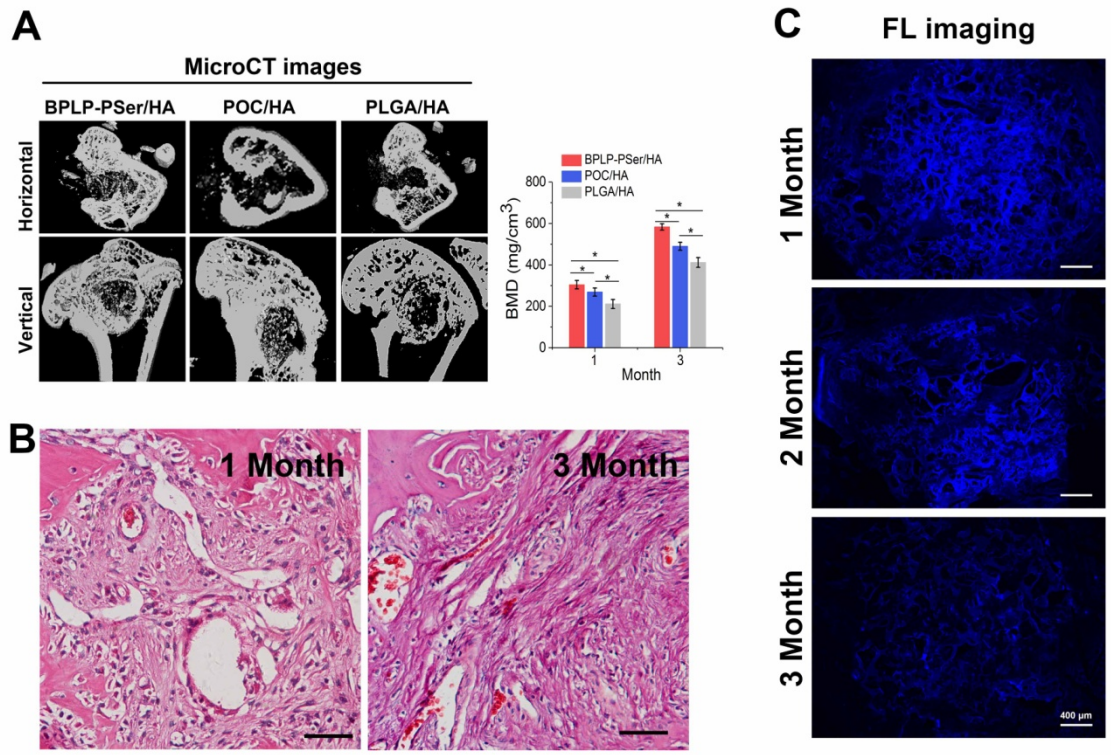


Figure S9 Additional *in vivo* results in femoral condyle defects. (A) MicroCT images of femoral condyle defects with BPLP-PSer/HA, POC/HA, and PLGA/HA MP scaffolds at 1 month after implantation with BMD analysis (Right; n=6 defects per group). (B) H&E staining of femoral condyle defects with no MPs implanted at 1 and 3 month after implantation (Scale bar: 50 μ m). (C) Fluorescent images of remaining BPLP-PSer/HA scaffold in tissue sections at 1, 2 and 3 month after implantation (Scale bar: 400 μ m).

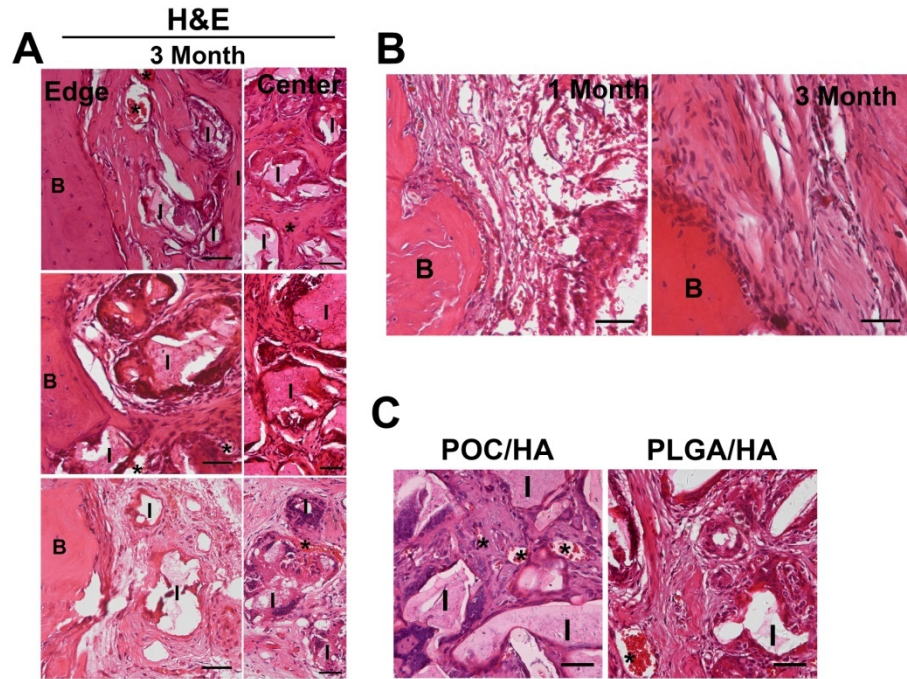


Figure S10 Additional *in vivo* results in cranial defects. (A) H&E staining of cranial defects treated with different Mps. Scale bars, 50 μ m. I indicates implants. B indicates bony front, * indicates new blood vessel. (B) H&E staining of cranial defects in the Control group with no MP scaffolds implanted (Scale bars, 50 μ m). (C) H&E staining of cranial defects treated with POC/HA and PLGA/HA Mps with blood vessels infiltrated at 1 month. Scale bars, 50 μ m, I indicates implants, B indicates bony front, * indicates new blood vessel.

References:

1. Oyane A, *et al.* (2003) Preparation and assessment of revised simulated body fluids. *Journal of biomedical materials research Part A* 65(2):188-195.